

3D-induced polar order and topological defects in growing bacterial populations

Takuro Shimaya* and Kazumasa A. Takeuchi†

Department of Physics, The University of Tokyo,
7-3-1 Hongo, Bunkyo-ku, Tokyo, 113-0033, Japan.

(Dated: July 26, 2022)

Rod-shaped bacteria, such as *Escherichia coli*, commonly live forming mounded colonies [1]. They initially grow two-dimensionally on a surface and finally achieve three-dimensional growth [2–8], which was recently reported to be promoted by $+1/2$ topological defects in motile populations [9]. In contrast, how cellular alignment plays a role in non-motile cases is largely unknown. Here, we investigate the relevance of topological defects in colony formation processes of non-motile *E. coli* populations, which is regarded as an active nematic system driven by cellular growth [10–13]. We show that while only $+1/2$ topological defects promote the three-dimensional growth in the early stage, cells gradually flow toward $-1/2$ defects as well, which leads to vertical growth around both defects. To explain our findings, we investigate three-dimensional cell orientations by confocal microscopy. We find that cells are strongly verticalized around defects and exhibit polar order characterized by asymmetric tilting of cells. We finally construct an active nematic theory by taking into account the three-dimensional orientation, and successfully explain the influx toward $-1/2$ defects. Our work reveals that three-dimensional cell orientations may result in drastic changes in properties of active nematics, especially those of topological defects.

Three-dimensional bacterial biofilms begin to form by cells growing in a two-dimensional plane [1]. In particular, rod-shaped bacteria, irrespective of whether they are motile or not, are aligned with each other and behave like an active nematic liquid crystal in a dense two-dimensional space [9–18]. For motile bacteria, it has recently been reported that $+1/2$ topological defects promote three-dimensional growth of *Myxococcus xanthus* populations [9]. Besides bacteria, it is known that topological defects also play decisive roles in populations of epithelial cells [19], neural stem cells [20], fibroblasts [21, 22] and actin fibers in *Hydra* [23]. However, for growing but non-motile bacteria, the relevance of topological defects to three-dimensional growth remains unknown. While some studies investigated how non-motile cells initiate three-dimensional growth [2–4, 6, 8, 24, 25], the relevance of local cell alignment has been overlooked.

Here, we observed colony formation processes of non-motile *E. coli* between a coverslip and a nutrient agar pad (see Fig. 1a and Methods). We first prepared cell suspensions at sufficiently low concentration for single cells to be isolated, and observed the growth of circular colonies in the two-dimensional plane (Fig. 1b). After a while, cells near the center of the colony were extruded from the bottom layer and entered the second layer (Supplementary Movie 1), similarly to previous studies [3, 6]. We then collected and analyzed the frame just before the first extruded cell appeared, from each of 60 independent colonies. To see whether cell extrusion is correlated with local cellular alignment, we measured the orientation of cells from the image intensity using the structure tensor method (see Methods and Supplementary Fig. 1a). We thereby obtained, at each position \mathbf{R} , the local cell orientation $\mathbf{n}(\mathbf{R})$ and the coherency parameter $C(\mathbf{R})$ which quantifies the degree of the local nematic order. Note that $C(\mathbf{R}) = 1$ if cells are perfectly

aligned, and $C(\mathbf{R}) = 0$ if cells are oriented to random directions. We first obtained the distribution of $C(\mathbf{R})$ in the region at a given normalized distance R/R_{\max} from the colony center, where R is the radial distance and R_{\max} is the approximate radius of each colony (Fig. 1c, blue boxplot). The result shows that $C(\mathbf{R})$ is constant near the center ($R/R_{\max} < 0.65$) and relatively high at the edge of the colony, which may be because cells at the periphery tend to align tangentially [2, 11]. We also collected 60 sets of the position and the coherency at the location where the first extrusion occurred in each colony (Fig. 1c, red symbols), and found higher extrusion frequency near the center as suggested by previous studies [3, 6]. Since the coherency $C(\mathbf{R})$ is essentially uniform near the center ($R/R_{\max} < 0.65$), we simply compare the distribution of $C(\mathbf{R})$ from all pixels in the region $R/R_{\max} < 0.65$ and that from 60 extrusion events (Fig. 1d top and Supplementary Fig. 1b). The result does not show significant difference between the two distributions, indicating that local cell alignment is unlikely to affect the first extrusion.

In contrast, based on a theoretical argument on torque balance around cells, it was proposed that the first extrusion is more likely to happen to short cells [6]. We therefore compare the distributions of cell lengths (Fig. 1d bottom and Supplementary Fig. 1c) and find that the extruded cells seem to be significantly shorter. These results suggest that, compared to the cell length or the radial position, the local cellular alignment does not seem to play a major role in the first extrusion in circular colonies. We also investigated the relation between the coherency and the cell length for each of the first extruded cells, and did not find significant correlation (Supplementary Fig. 1d). This suggests that, in such isolated expanding colonies, the in-plane stress which becomes strongest at the center due to cell growth [6, 26–28] in-

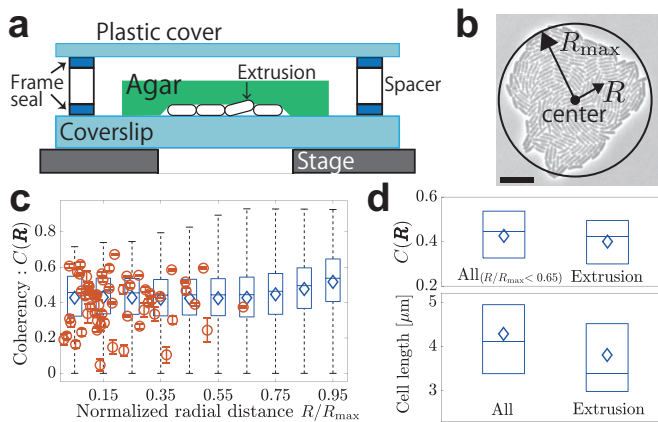


FIG. 1. Results on circular colonies formed from a few cells. We investigated the first extruded cell (labeled as extrusion) in each of 60 colonies. **a**, Experimental setup. Bacterial cells were between a coverslip and a nutrient agar pad. **b**, A circular colony formed from a single cell (see also Supplementary Movie 1). The scale bar is $10 \mu\text{m}$. R_{max} is defined as the radius of a circle that has the same area as the colony (see Methods). **c**, Spatial distribution of the coherence $C(\mathbf{R})$ in the region at a given R/R_{max} (boxplots) and for the first extruded cells (red circles). The boxplots in this paper indicate the median by the horizontal lines, the lower and upper quartiles by the lower and upper box edges, respectively, the minimum and maximum by the error bars, and the mean value by the diamonds. The error bars of the red circles indicate the standard deviation of $C(\mathbf{R})$ over the pixels contained in the extruded cells (see Methods). The uncertainty of the position is smaller than the symbol size. **d**, Comparison of $C(\mathbf{R})$ (top) and the cell length (bottom) between all cells and the first extruded cells. For the coherence distribution, data for all cells were collected in the region $R/R_{\text{max}} < 0.65$.

deed constitutes a major factor in the start of the three-dimensional growth, as reported earlier [3, 6], regardless of topological defects.

However, colonies are not necessarily isolated when initial cells are not too dilute. If the initial concentration is relatively high, several microcolonies will expand simultaneously, collide, and merge. We can expect more spatially uniform in-plane stress in this case. To study a model case for such dense situations, here we started with densely and uniformly distributed cells by using cell suspension at relatively high concentration (see Methods). Cells then immediately filled the two-dimensional plane (Fig. 2a) and after a short while cells started to rise almost simultaneously, turning toward the three-dimensional space (Supplementary Movie 2). Cells continued growing afterward, but even after 14 hours, the tilt angle of the cells was moderate, typically $\sim 10^\circ$ (see Fig. 4b which will be discussed later). We can therefore regard this as a quasi-two-dimensional active nematic system.

To test the relevance of cell alignment to the three-dimensional growth, we investigate how cells rearranged

around topological defects. Detecting defects from the two-dimensional cell orientation $\mathbf{n}(\mathbf{R}, t)$ on the bottom layer (Supplementary Fig. 2a-d), first we found that the density of defects initially increased, then stayed approximately constant from $t \approx 30$ min (Supplementary Fig. 2e), where $t = 0$ is the time at which cells filled the bottom layer. Then we measured the velocity field around defects by particle image velocimetry (PIV) (see Methods). In Fig. 2b,c and Supplementary Fig. 3a,b, the arrows show the velocity field $\mathbf{v}^\pm(\mathbf{r}, t)$ around $\pm 1/2$ defects, time-averaged over $30 \text{ min} \leq t \leq 105 \text{ min}$, where \mathbf{r} indicates the position relative to the defect and the double sign corresponds to the sign of the defect. While the structure of $\mathbf{v}^\pm(\mathbf{r}, t)$ resembles those around defects in typical extensile active nematic systems [29], their divergence $\nabla \cdot \mathbf{v}^\pm(\mathbf{r}, t)$ (color map of Fig. 2b,c; see also Supplementary Fig. 3c-e) reveals a distinguished character of our system: we found negative divergence around both types of defects, not only around $+1/2$ defects (Fig. 2b) as previously reported for systems of motile cell populations [9, 14, 15, 19, 20, 22], but even around $-1/2$ defects (Fig. 2c), as opposed to those earlier studies. Since negative divergence represents influx of cells, this implies that cells are moving toward both types of defects in the bottom layer and pushed out upward. To inspect the time evolution of this influx, in Fig. 2d, we examined the mean radial velocity at a distance r from $+1/2$ or $-1/2$ defect, $\bar{v}_r^\pm(r, t) \equiv \frac{1}{2\pi} \oint d\phi v_r^\pm(\mathbf{r}, t)$, where $v_r^\pm(\mathbf{r}, t)$ is the radial component of the velocity $\mathbf{v}^\pm(\mathbf{r}, t)$ at polar coordinates $\mathbf{r} = (r, \phi)$ centered at the defect. Then we find that $v_r^+(r)$ around $+1/2$ defects (Fig. 2e) is essentially negative all the time, but the depth of the minimum decreased with increasing time. This may be because of decay of the overall flow speed throughout the colony due to nutrient starvation (Supplementary Fig. 3f and Supplementary Movie 2). In contrast, $v_r^-(r)$ was initially positive for all r , but grew in the negative direction near the defect and remained negative. To see the time evolution of the strength of the influx near the defects more clearly, we plotted $\min_{r < r_0} \bar{v}_r^\pm(r)$ with $r_0 = 2 \mu\text{m}$ (Fig. 2g). While the strength of the influx around the $+1/2$ defect monotonically decreased, that around the $-1/2$ defect increased until $t \simeq 25$ min.

As we have already mentioned, the influx around topological defects can push cells upward. We directly investigated the effect of topological defects on the colony height by confocal microscopy (Methods and Fig. 3a). To take high quality images without photobleaching, we took images only once, long (14 hours) after cells had filled the bottom layer. We first detected topological defects in the bottom layer of the three-dimensional colony, and obtained the colony height on the defects (Methods). For comparison, we randomly selected locations sufficiently far from topological defects, and measured the colony height on the selected points. We found that the mean colony height is relatively high at the positions of the

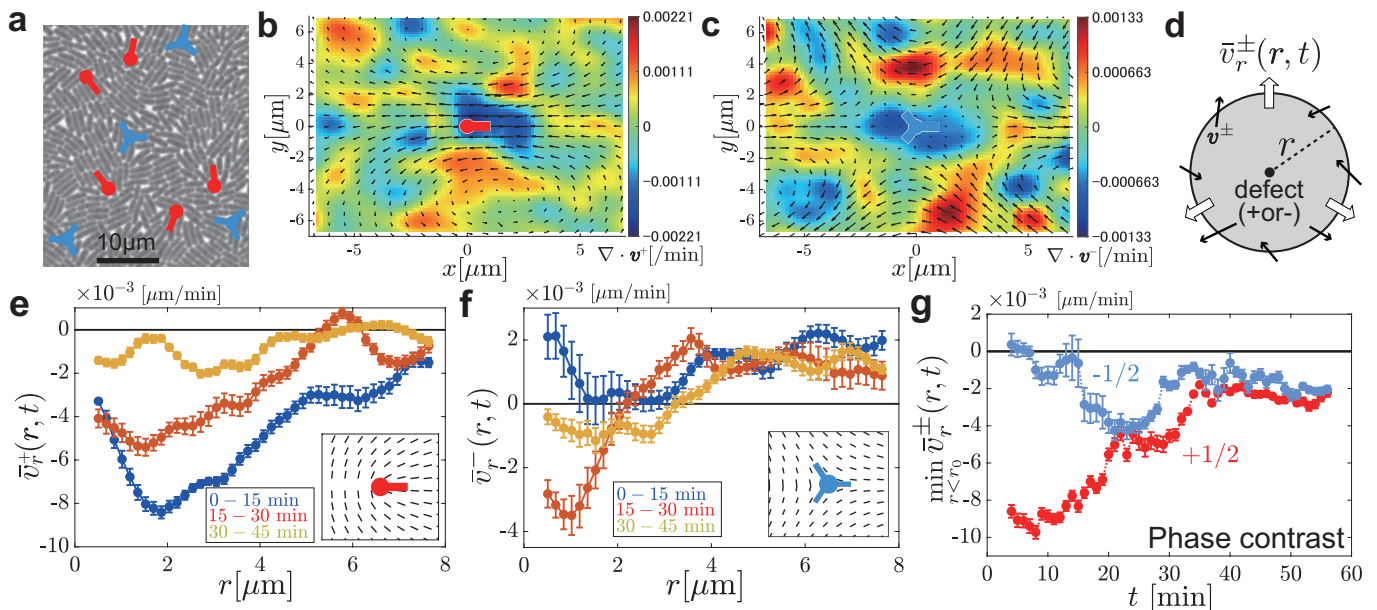


FIG. 2. Results on uniform colonies formed from numerous cells observed by phase contrast microscopy. The time interval of the time-lapse observation was 1 min. **a**, phase-contrast image of cells taken at $t = 0$, i.e., at the moment when cells filled the bottom layer. Red comets and blue trefoils indicate $+1/2$ and $-1/2$ defects, respectively. The arms of the symbols reflect the structure of the director field as illustrated in the inset of **(e,f)**. See also Supplementary Movie 2. **b,c**, Velocity field $\mathbf{v}^\pm(\mathbf{r}, t)$ (black arrows) and divergence field $\nabla \cdot \mathbf{v}^\pm(\mathbf{r}, t)$ (color maps) around $+1/2$ defects (**b**) and $-1/2$ defects (**c**). Average was taken over all defects detected in each frame during $30 \text{ min} \leq t \leq 105 \text{ min}$, then time average was taken. See Methods for details. **d**, Schematic illustration of the definition of the mean radial velocity $\bar{v}_r^\pm(r, t)$, which corresponds to the net flow from a circular region of radius r centered at the defect. **e,f**, Time evolution of the mean radial velocity $\bar{v}_r^\pm(r, t)$ around $+1/2$ defects (**e**) and $-1/2$ defects (**f**). Here we used the velocity field averaged over $0 \text{ min} \leq t \leq 15 \text{ min}$, $15 \text{ min} \leq t \leq 30 \text{ min}$, and $30 \text{ min} \leq t \leq 45 \text{ min}$. The error bars indicate the time average of the standard error evaluated from each frame. **g**, Time evolution of the minimum of $\bar{v}_r^\pm(r, t)$ in the region $r < r_0 = 2 \mu\text{m}$ near the defect. The moving average taken from $(t - 5 \text{ min})$ to $(t + 5 \text{ min})$ is shown with the corresponding error bar.

$\pm 1/2$ defects (Fig. 3b). More quantitatively, we evaluated the significance by Student's t-test, which can be used thanks to roughly Gaussian distributions observed in the colony height data (Supplementary Fig. 4a-c). The p-value of the hypothesis that the colony height distribution on the defects is identical to that in the absence of defects is 0.012 for the $+1/2$ defects, and 0.028 for the $-1/2$ defects. These results demonstrate that topological defects significantly promote the vertical growth of colonies.

To seek for a possible mechanism of the influx toward $-1/2$ defects, we developed a theory based on two-dimensional extensile active nematics, extended to incorporate characteristics of growing non-motile colonies we observed. Following earlier studies [9, 20], we describe the cell alignment by the nematic order tensor $\mathbf{Q}(\mathbf{r}, t) \equiv S(2\mathbf{n} \otimes \mathbf{n} - \mathbf{1})$, with the scalar nematic order parameter $S(\mathbf{r}, t)$, the director field $\mathbf{n}(\mathbf{r}, t)$, and the identity matrix $\mathbf{1}$ (see Methods). As cells elongate along their major axis, interacting with nearby cells, they exert the extensile active stress $\boldsymbol{\sigma} = -a_n \mathbf{Q}$ with the active stress coefficient $a_n (> 0)$. This stress induces the force $\mathbf{f} = \nabla \cdot \boldsymbol{\sigma}$ and drives the velocity field $\mathbf{v}(\mathbf{r}, t)$. In the over-

damped and low Reynolds number limit, this active force is balanced by the friction originating from cell-substrate interaction, giving the following linearized equation

$$\boldsymbol{\xi} \mathbf{v} = \nabla \cdot (-a_n \mathbf{Q}), \quad (1)$$

with the friction tensor $\boldsymbol{\xi}$. We assume that friction is anisotropic depending on the cell alignment: $\boldsymbol{\xi} = \xi_0(\mathbf{1} - \epsilon \mathbf{Q})$ with the friction anisotropy ϵ . As suggested in Ref. [30], we may reasonably assume that it is easier for *E. coli* cells to slide along their longitudinal axis, hence $\epsilon > 0$. Setting \mathbf{Q} with the typical director configurations for $\pm 1/2$ defects and the core radius determined experimentally from the coherency (see Methods and Supplementary Fig. 5a,b), we calculated the mean radial velocity $\bar{v}_r^\pm(r)$ (Fig. 4a inset, dotted lines), which shows influx only for $+1/2$ defects and outflux only for $-1/2$ defects. Therefore, to explain the experimentally observed influx around $-1/2$ defects, we need to extend the existing theoretical framework described so far. One may consider that this influx might be due to the density heterogeneity, in particular small voids observed at $-1/2$ defects in the early stage of the process (Supplementary Movie 2). However, this is unlikely to explain the observed influx

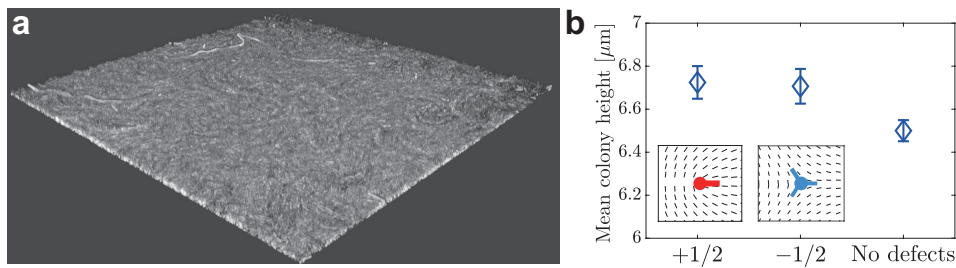


FIG. 3. Morphology of uniform colonies formed from numerous cells observed by end-point confocal microscopy. The confocal data were taken 14 hours after the cells had filled the bottom layer. **a**, A three-dimensional image of colonies ($184.52 \mu\text{m} \times 184.52 \mu\text{m}$ square). **b**, Mean colony height on defects and that far from defects. The data for the defects were extracted from hundreds of independent defects sufficiently far from each other. For the colony height far from defects, we randomly picked up 1000 points which were sufficiently far from any defect (see Methods). The error bars indicate the standard error from the ensemble averaging. See also Supplementary Fig. 4a-c for the colony height distributions.

which developed at later times, because more voids existed at earlier times. We also attempted to add a growth term to the hydrodynamic equation, but we could not reproduce the influx toward $-1/2$ defects (see Supplementary Information).

Instead of the growth and the density heterogeneity, here we focus on the three-dimensional orientations of the cells, because the influx toward $-1/2$ defects became strong when cells began to tilt three-dimensionally (Fig. 2f and Supplementary Movie 2). We consider that the local active stress and the friction anisotropy in our two-dimensional description may be weakened when cells are tilted three-dimensionally. More quantitatively, we assume that the local active stress coefficient and the friction anisotropy are given by $a_n(\mathbf{r}, t) = a_n^0 \cos \theta_n(\mathbf{r}, t)$ and $\epsilon(\mathbf{r}, t) = \epsilon_0 \cos \theta_n(\mathbf{r}, t)$, respectively, with constants a_n^0 and ϵ_0 , if cells at position \mathbf{r} are tilted by angle $\theta_n(\mathbf{r}, t)$ from the horizontal plane (see the illustration in Fig. 4b). We measured $\theta_n(\mathbf{r}, t)$ at a late time t experimentally from the end-point confocal data (Methods). By the structure tensor method for the three-dimensional space, we obtained $\theta_n^\pm(\mathbf{r})$ around $\pm 1/2$ defects (Fig. 4b and Supplementary Fig. 4e,f). Remarkably, we found that three-dimensional tilting was strongest at the core of both defects, which results in smaller active stress coefficient there. The peak of $\theta_n^\pm(\mathbf{r})$ was well approximated by a Gaussian function centered at the defect core plus a constant (Fig. 4b), and $\theta_n^\pm(\mathbf{r})$ turned out to be essentially isotropic (Supplementary Fig. 4e,f). Using this, we numerically and analytically solved Eq. (1) and revealed the emergence of the influx toward $-1/2$ defects (Fig. 4a inset, blue solid line; see also Supplementary Information and Supplementary Fig. 5c). However, the strength of the influx obtained thereby (Fig. 4a inset, blue solid line) was significantly smaller than the experimental result (Fig. 4a main, blue symbols). This led us to seek for another key factor for the influx toward $-1/2$ defects.

Here, we propose a key mechanism for the strong influx toward $-1/2$ defects (Fig. 2f,g). So far, we assumed that

active force is induced only by nematic alignment. However, when cells are tilted three-dimensionally, the sign of the tilt angle θ_p may break the nematic symmetry and make it possible to develop polar order (Fig. 4c). Such polar order was indeed observed in experiments on vibrated granular rods densely packed in three-dimensional space [31, 32]. They also showed that if rod particles were tilted and aligned as shown in Fig. 4c, the particles were transported in the direction of the upper end of the rods. Inspired by this possibility, we measured $\theta_p(\mathbf{r})$ around both types of defects by end-point confocal microscopy. Figure 4d shows $\theta_p(\mathbf{r})$ on the $+x$ -axis, which is defined in such a way that the director is radial along this axis, i.e., $(n_x, n_y) = (1, 0)$. The result shows non-vanishing $\theta_p(\mathbf{r})$ for both $\pm 1/2$ defects, demonstrating the emergence of the polar order in our growing bacterial populations. Interestingly, we found $\theta_p(\mathbf{r}) > 0$ (upper end oriented outward) for $+1/2$ defects and $\theta_p(\mathbf{r}) < 0$ (upper end oriented inward) for $-1/2$ defects. This latter result implies that the force \mathbf{f}_p induced by the polar order acts toward $-1/2$ defects and contributes to the influx. Following the earlier result on vibrated rods [32], we assumed $\mathbf{f}_p \propto n\theta_p$ and visualize this polarity-induced force field around topological defects in Fig. 4e,f. This shows that the polarity-induced force around $-1/2$ defects indeed acts toward the defect, almost everywhere (Fig. 4f).

To quantitatively deal with the mean radial velocity, we incorporate the contribution of the polarity-induced force \mathbf{f}_p into Eq. (1). With $a_n = a_n^0 \cos \theta_n$ and $\boldsymbol{\xi} = \xi_0(\mathbf{1} - \epsilon_0 \cos \theta_n \mathbf{Q})$, we obtain the following equation:

$$\xi_0(\mathbf{1} - \epsilon_0 \cos \theta_n \mathbf{Q})\mathbf{v} = \nabla \cdot (-a_n^0 \cos \theta_n \mathbf{Q}) + a_p^0 \theta_p \mathbf{n}. \quad (2)$$

Then we experimentally measured $\theta_n(\mathbf{r}, t)$, $\theta_p(\mathbf{r}, t)$ and $\mathbf{Q}(\mathbf{r}, t)$ for $\pm 1/2$ defects by time-lapse confocal observation, using a time period showing the strongest influx toward $-1/2$ defects (see Methods, Supplementary Movie 3, and Supplementary Fig. 6). We are to determine three unknown parameters, $a_n^0 S_0 / \xi_0$, a_p^0 / ξ_0 and ϵS_0 , where S_0 is the scalar nematic order parameter sufficiently far from defects. The friction anisotropy

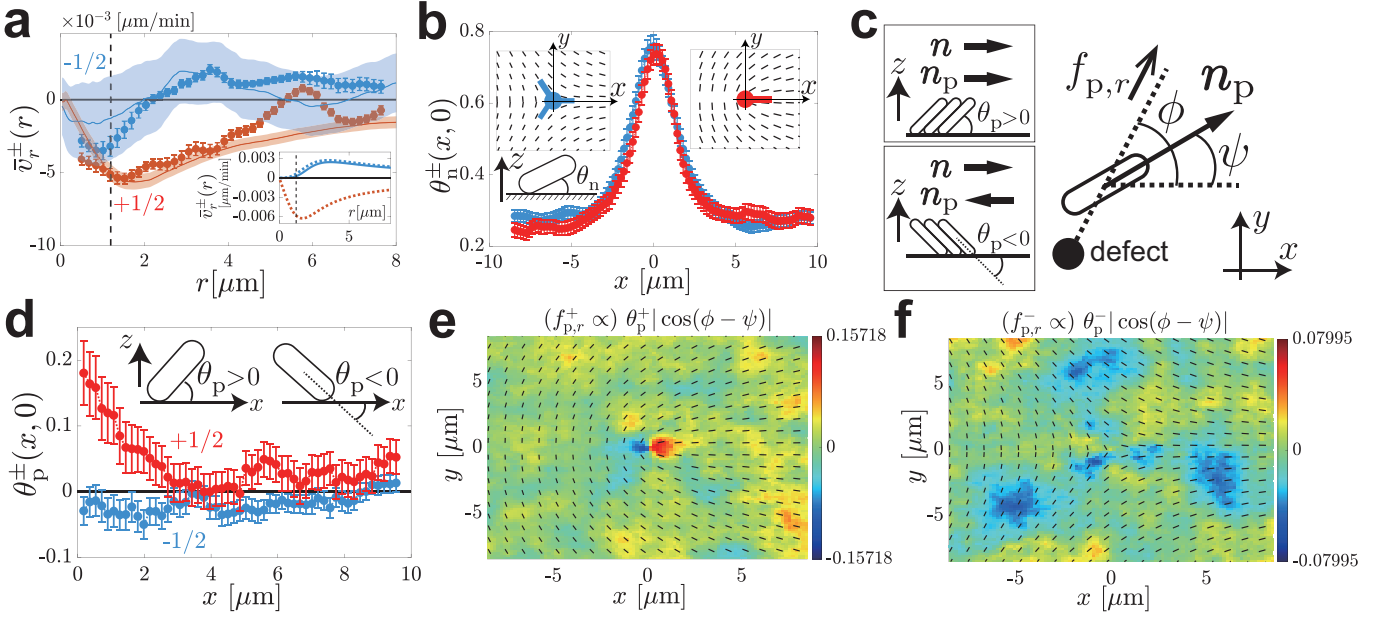


FIG. 4. Results on uniform colonies formed from numerous cells observed by end-point confocal microscopy and corresponding theoretical analysis. The double sign \pm corresponds to the sign of the defects. **a**, Comparison of the mean radial velocity $\bar{v}_r^\pm(r)$ obtained experimentally (symbols) and that evaluated theoretically from Eq. (2). The solid lines represent the theoretical result from Eq. (2), which takes into account the effect of three-dimensional tilting and polar order. The shaded bands indicate the range of uncertainty, evaluated from the standard error of the experimental data of $\theta_p^\pm(r, t)$, which were used in the theoretical evaluation. The parameter values were $\epsilon_0 = 0.25$, $a_n^0/\xi_0 = 0.055 \mu\text{m}^2/\text{min}$, and $a_p^0/\xi_0 = 0.8 \mu\text{m}/\text{min}$ (see Methods). The displayed experimental data (symbols) are results from the phase contrast observation during $15 \text{ min} \leq t \leq 30 \text{ min}$, when the influx toward $-1/2$ defects was strongest (the same data as in Fig. 2e,f). The vertical dashed line indicates the defect core radius $r_S = 1.2 \mu\text{m}$ (see Methods and Supplementary Fig. 5a,b). (Inset) The dotted lines represent the result from Eq. (1) with constant $\epsilon = \epsilon_0$ and $a_n = a_n^0$ ($\epsilon = 0.25$, $a_n/\xi_0 = 0.055 \mu\text{m}^2/\text{min}$, $r_S = 1.2 \mu\text{m}$; see Methods). The solid line is the result for $-1/2$ defects with nematic tilting, i.e., $a_n = a_n^0 \cos(\theta_n^\pm(\mathbf{r}))$, but without polar order ($\theta_n^\pm(r, \phi) = \theta_n^\infty + (\theta_n^0 - \theta_n^\infty) \exp(-r^2/r_\theta^2)$ with $\theta_n^\infty = 0.3$ and $\theta_n^0 = 0.75$, with the other parameters left unchanged; see Methods). **b**, Nematic tilt angle $\theta_n^\pm(r)$ around $\pm 1/2$ defects. The results on the x -axis, i.e., $\mathbf{r} = (x, 0)$, are displayed. To obtain them, we first measured the three-dimensional cell orientations by the structure tensor method and obtained the non-negative tilt angle with respect to the xy plane. We then took the ensemble average over all defects. The error bars indicate the standard error from the ensemble averaging. The two insets illustrate the definition of the x -axis for $+1/2$ (right inset) and $-1/2$ (left inset) defects. **c**, Illustrations of the polar tilt angle θ_p and the polar director $\mathbf{n}_p = \mathbf{n}\theta_p/|\theta_p|$ (left panels), and that of the radial component of the polarity-induced force, $f_{p,r}$ (right panel). The polar tilt angle θ_p takes a positive (negative) value if the cell end at the head (tail) of the nematic director \mathbf{n} is lifted above the substrate. Note that θ_p changes its sign if \mathbf{n} is reversed, but \mathbf{n}_p remains unchanged, always pointing the direction of the upper end of the cell. The polarity-induced force $\mathbf{f}_p \propto \mathbf{n}\theta_p$ is oriented toward \mathbf{n}_p (see Methods). Since $\mathbf{f}_p^\pm \propto \theta_p^\pm \mathbf{n}$ with $\mathbf{n} = (\cos \psi, \sin \psi)$, we have $f_{p,r}^\pm \propto |\theta_p| \cos(\phi - \psi)$. **d**, The polar tilt angle θ_p^\pm measured on the $+x$ -axis of $\pm 1/2$ defects (see **b** for the definition of the axis). Sign of θ_p^\pm is chosen such that the director $\mathbf{n}(\mathbf{r})$ on the $+x$ -axis is $(n_x, n_y) = (1, 0)$ (see Methods). The ensemble average over all defects is shown. The error bars indicate the standard error from the ensemble averaging. **e, f**, $\theta_p^\pm |\cos(\phi - \psi)|$, which is proportional to the radial component of the polarity-induced force, $f_{p,r}$, around the $+1/2$ defect (**e**) and the $-1/2$ defect (**f**). The negative radial component indicates that the polarity-induced force is directed toward the defect. The black rods represent the nematic director field $\mathbf{n}(\mathbf{r})$.

ϵ turned out to hardly affect $\bar{v}_r^\pm(r, t)$, so that we are left with two effective parameters, $a_n^0 S_0/\xi_0$ and a_p^0/ξ_0 . While the nematic contribution solely could not reproduce the experimental result as we described above, we found, remarkably, that the addition of the polar contribution a_p^0/ξ_0 strengthened the influx toward $-1/2$ defects significantly (Fig. 4a, solid curves). In particular, we were able to find such values of $a_n^0 S_0/\xi_0$ and a_p^0/ξ_0 that satisfactorily reproduced the experimental data of both $\bar{v}_r^\pm(r)$ and $\bar{v}_r(r)$ (see Methods). This demonstrates that the three-dimensional tilting and resulting polar order were

the keys to understand the unusual influx toward $-1/2$ defects we observed in our growing non-motile bacterial populations.

In summary, we showed the relevance of topological defects to the three-dimensional growth of growing non-motile *E. coli* populations, unveiling the emergence of polar order and resulting novel properties endowed with this active nematic system. When a colony formation was initiated by numerous cells, cells started to tilt three-dimensionally a short while after they filled the bottom layer. Since then, the net influx toward both $+1/2$

and $-1/2$ defects appeared, which promoted the vertical growth of colonies. The influx toward $-1/2$ defects was unexpected from the existing theory of active nematics, but we revealed that this resulted from the three-dimensional tilting of cells around defects and the polar order induced thereby. We extended the active nematics theory to incorporate these effects and successfully accounted for the experimental observation. We therefore demonstrated the role of $-1/2$ defects in the formation of three-dimensional structures of cell populations, which has been overlooked compared to that of $+1/2$ defects supported by many recent studies [9, 14, 15, 19, 20, 22]. The relevance of $-1/2$ defects, as well as the possibility of the polar order and resulting novel properties of active nematics, may also shed a new light on other cellular systems with three-dimensional structures and beyond.

METHODS

Strains, culture media and sample setup

We used a wild-type *E. coli* strain MG1655 and its mutant MG1655-pZA3R-EYFP that contains a plasmid pZA3R-EYFP expressing enhanced yellow fluorescent proteins. We used LB broth (tryptone 1 wt%, sodium chloride 1 wt% and Yeast extract 0.5 wt%) and TB+Cm medium (tryptone 1 wt% , sodium chloride 1 wt% and chloramphenicol 165 $\mu\text{g}/\text{ml}$). To prepare nutrient agar pads, we added agar powder to medium, solidified it by a microwave oven, then cut it into squares of size 13 mm \times 13 mm. For each observation, we inoculated bacterial suspension on a coverslip and put an agar pad on the suspension. We then attached the following on the coverslip, surrounding the agar pad, to prevent the agar from drying out (Fig. 1a): a frame seal (SLF0601, Bio-Rad), a 3D printed PLA spacer (5 mm height, hollow square, inner dimensions 14 mm \times 14 mm and outer dimensions 22 mm \times 22 mm), another frame seal, then a plastic cover that enclosed the inner region. Details on the strain and the culture condition in each experiment are provided below. The *E. coli* strains we used did not swim at all in our experimental conditions (Supplementary Movies 1-3).

Phase contrast observation of circular colonies formed from a few cells

We used the wild-type strain MG1655. Before the time-lapse observation, we inoculated the strain from a glycerol stock into 2 ml LB broth in a test tube. After shaking it overnight at 37 $^{\circ}\text{C}$, we transferred 20 μl of the incubated suspension to 2 ml fresh LB broth and cultured it until the optical density (OD) at 600 nm wavelength reached 0.1-0.3. The bacterial suspension was finally di-

luted to OD = 0.01, and 1 μl of the suspension was inoculated between the coverslip and the LB agar pad (2.0 wt% agar).

The sample was placed on the microscope stage, in an incubation box maintained at 37 $^{\circ}\text{C}$. The microscope we used was Leica DMI8, equipped with a 63x (N.A. 1.30) oil immersion objective and a CCD camera (Leica DFC3000G), and operated by Leica LasX. The image pixel size was $\approx 0.17 \mu\text{m}$. We carried out time-lapse observations with the time interval 1 min for 30 isolated colonies, which started to form from a few cells. We repeated the experiments twice and acquired data from 60 colonies in total. From each colony, we chose the frame right before the first extrusion of a cell from the bottom layer took place. We used 60 such images from the 60 colonies for analysis. For each colony, we binarized the image, and obtained the area A by the total number of pixels, the center position by the center of mass, and the radius R_{max} by $\pi R_{\text{max}}^2 = A$, using the regionprops function of MATLAB. The first extruded cell was detected manually, by using a black spot that a tilted cell exhibits in the phase-contrast image (see Supplementary Movie 1). We manually labeled pixels contained in each extruded cell, and obtained the position as well as the mean and the standard deviation of the coherency over the labeled pixels (see the section ‘‘Analysis of phase-contrast images’’ for the method to evaluate the coherency). To obtain the spatial dependence of the coherency shown by boxplots in Fig. 1c, we divided the space into regions bordered by concentric circles, with the radii that increased by $R/R_{\text{max}} = 0.1$. The length of cells was evaluated manually from the major axis of each cell by using a painting software.

Phase contrast observation of uniform colonies formed from numerous cells

We used the wild-type strain MG1655. We cultured bacteria in the same way as for the observation of circular colonies. The bacterial suspension was finally concentrated to OD = 5 by a centrifuge, and 1 μl of the suspension was inoculated between the coverslip and the LB agar pad (1.5 wt% agar).

The imaging process and the condition during the observation were the same as those for the observation of circular colonies. We carried out time-lapse observation with the time interval 1 min for 30 separate regions of dimensions 110.03 $\mu\text{m} \times 81.97 \mu\text{m}$. For each region, we determined the frame at $t = 0$, i.e., the frame in which cells filled the observation area for the first time. We then measured the cell orientation $\mathbf{n}(\mathbf{R})$ and detected topological defects in all frames, by the method described below. We used isolated topological defects only, each separated by a distance longer than 9.5 μm from the nearest defect. As a result, we obtained hundreds of defects for

each time.

Analysis of phase-contrast images

Using phase-contrast images from circular and uniform colonies, we measured the cell orientation $\mathbf{n}(\mathbf{R})$ and the coherency $C(\mathbf{R})$ by the structure tensor method. The image pixel size was $\approx 0.17 \mu\text{m}$. After sharpening the images by a high-pass filter, we calculated the structure tensor $J(\mathbf{R})$ at a given pixel $\mathbf{R} = (X, Y)$ by

$$J(\mathbf{R}) = \begin{pmatrix} [\Delta_X I, \Delta_X I]_{\mathbf{R}}, & [\Delta_Y I, \Delta_X I]_{\mathbf{R}} \\ [\Delta_X I, \Delta_Y I]_{\mathbf{R}}, & [\Delta_Y I, \Delta_Y I]_{\mathbf{R}} \end{pmatrix}, \quad (3)$$

with the image intensity $I(X, Y)$, $\Delta_X I \equiv I(X + 1, Y) - I(X - 1, Y)$, $\Delta_Y I \equiv I(X, Y + 1) - I(X, Y - 1)$, and $[g, h]_{\mathbf{R}} \equiv \sum_{(X', Y') \in \text{ROI}_{\mathbf{R}}^{\ell}} g(X', Y') h(X', Y') f_{\mathbf{R}}^{\sigma}(X', Y')$. Here, the summation is taken over a region of interest $\text{ROI}_{\mathbf{R}}^{\ell}$, which is a square of size $\ell \approx 6.8 \mu\text{m}$ (40 pixels) centered at \mathbf{R} , and $f_{\mathbf{R}}^{\sigma}(X', Y')$ is the Gaussian kernel defined by $f_{\mathbf{R}}^{\sigma}(X', Y') \equiv \exp[-\frac{(X' - X)^2 + (Y' - Y)^2}{2\sigma^2}]$ with $\sigma = 1.7 \mu\text{m}$. Then the cell orientation $\mathbf{n}(\mathbf{R})$ is given by the eigenvector of $J(\mathbf{R})$ associated with the smallest eigenvalue $\lambda^{\min}(\mathbf{R})$. The orientation $\mathbf{n}(\mathbf{R})$ can also be represented by angle $\psi(\mathbf{R})$ such that $\mathbf{n} = \pm(\cos \psi, \sin \psi)$ with $-\pi/2 \leq \psi < \pi/2$. The coherency parameter $C(\mathbf{R})$, which quantifies the degree of the local nematic order, is given by

$$C(\mathbf{R}) = \frac{\lambda^{\max}(\mathbf{R}) - \lambda^{\min}(\mathbf{R})}{\lambda^{\max}(\mathbf{R}) + \lambda^{\min}(\mathbf{R})}, \quad (4)$$

with the largest eigenvalue $\lambda^{\max}(\mathbf{R})$.

To detect topological defects, we first calculated the nematic order parameter by

$$S(\mathbf{R}) = \langle \sin 2\psi \rangle_{\text{ROI}_{\mathbf{R}}^{\ell}}^2 + \langle \cos 2\psi \rangle_{\text{ROI}_{\mathbf{R}}^{\ell}}^2, \quad (5)$$

where $\langle \cdot \rangle_{\text{ROI}_{\mathbf{R}}^{\ell}}$ denotes the spatial average within $\text{ROI}_{\mathbf{R}}^{\ell}$. Then we located the positions of local minima of $S(\mathbf{R})$ as candidates of topological defect cores. For each candidate point, we calculated the topological charge $q = \frac{1}{2\pi} \oint_{\mathcal{C}} d\psi$, where \mathcal{C} is a square closed path with a side of about $3.4 \mu\text{m}$ (20 pixels) centered at the candidate point. The candidate point is regarded as a topological defect if $q = \pm 1/2$, and dismissed otherwise. To determine the angle of the arm of each defect (Fig. 2e,f inset), we used the profile of $|\psi - \phi|$ on \mathcal{C} , where ϕ is the azimuth with respect to the defect core. A single minimum of $|\psi - \phi|$ exists for each $+1/2$ defect, while there are three local minima for each $-1/2$ defect. Each minimum point corresponds to an arm of the defect. Blue trefoils indicating $-1/2$ defects in Fig. 2a, Supplementary Fig. 2d and Supplementary Movie 2 were drawn by setting one of the arms of the trefoil at the angle of the global minimum,

with the other two arms added by rotating the first arm by 120° .

For uniform colonies, we also measured the velocity field of the cells around the detected defects, by particle image velocimetry (PIV). For this, we used MatPIV [33] (open source PIV toolbox for MATLAB), with the PIV window set to be a square of size $\approx 2.7 \mu\text{m}$ (16 pixels). To take averages over defects, for each defect we rotated the image so that the defect arm was oriented in the positive direction of the x -axis. For $-1/2$ defects, we did this rotation for each of their three arms, and all of the resulting velocity fields were used for the ensemble average. We thereby obtained the ensemble-averaged velocity field $\mathbf{v}(\mathbf{r}, t)$, as a function of the coordinate $\mathbf{r} = (x, y)$ relative to the defect, and time t .

The divergence of $\mathbf{v}(\mathbf{r}) = (u(\mathbf{r}), v(\mathbf{r}))$ was calculated as follows (here we omit t from the argument for simplicity). We first obtained $D(\mathbf{r}) = \frac{u(x+1, y) - u(x-1, y)}{2\delta} + \frac{v(x, y+1) - v(x, y-1)}{2\delta}$ with the pixel size $\delta \approx 0.17 \mu\text{m}$. We then calculated the divergence field by

$$(\nabla \cdot \mathbf{v})(\mathbf{r}) = \frac{\sum_{(x', y') \in \text{ROI}_{\mathbf{r}}^{\ell}} D(\mathbf{r}') f_{\mathbf{r}}^{\sigma}(x', y')}{\sum_{(x', y') \in \text{ROI}_{\mathbf{r}}^{\ell}} f_{\mathbf{r}}^{\sigma}(x', y')}, \quad (6)$$

where $\text{ROI}_{\mathbf{r}}^{\ell}$ and the Gaussian kernel $f_{\mathbf{r}}^{\sigma}(x', y')$ were defined as above, but with $\ell \approx 2.7 \mu\text{m}$ (16 pixels) and $\sigma \approx 0.68 \mu\text{m}$ (5 pixels).

Confocal observations of uniform colonies formed from numerous cells

We used the mutant strain MG1655-pZA3R-EYFP that expresses enhanced yellow fluorescent proteins. Before the observations, we inoculated the strain from a glycerol stock into 2 ml TB+Cm medium in a test tube. After shaking it overnight at 37°C , we transferred 20 μl of the incubated suspension to 2 ml fresh TB+Cm medium and cultured it until OD at 600 nm wavelength reached 0.1-0.5. The bacterial suspension was finally concentrated to OD = 5 by a centrifuge, and 1 μl of the suspension was inoculated between the coverslip and the agar pad (1.5 wt% agar).

The sample was placed on the microscope stage, in a stage-top incubator maintained at 37°C . The microscope we used was Leica SP8, equipped with a 63x (N.A. 1.40) oil immersion objective and operated by Leica LasX. The data shown in Fig. 4 and Supplementary Fig. 4 were obtained by an end-point observation, in which we cultured the colonies without excitation light until 14 hours after the cells had filled the observation area. We captured three-dimensional images of size $184.52 \mu\text{m} \times 184.52 \mu\text{m} \times 16 \mu\text{m}$ from 20 separate regions. For the data shown in Supplementary Fig. 7, we carried out a time-lapse observation, obtaining images of size $184.52 \mu\text{m} \times 184.52 \mu\text{m} \times 6.4 \mu\text{m}$ from 4 separate

regions with the time interval 15 min. The image pixel size was $\approx 0.18 \mu\text{m}$ in the xy plane and $0.16 \mu\text{m}$ along the z -axis.

The detection of topological defects in the bottom layer was carried out in the same manner as that for phase-contrast observations. For each region, we chose the plane corresponding to the bottom layer and carried out the two-dimensional structure tensor method described above, with the ROI size $\ell \approx 7.2 \mu\text{m}$ (40 pixels) and the characteristic length of the Gaussian filter, $\sigma \approx 1.8 \mu\text{m}$ (10 pixels). We thereby obtained the two-dimensional locations of all defects and their signs.

To investigate the dependence of the colony height on topological defects, we picked up hundreds of isolated defects, separated by a distance longer than $9 \mu\text{m}$ from the nearest defect. For comparison, we also randomly selected 1000 points which are separated more than $9 \mu\text{m}$ from defects. For a given position in the xy -plane, we obtained the image intensity profile along the z -axis. The height was then determined by the length of the region whose intensity was higher than 20% of the maximum intensity in this profile.

The three-dimensional tilting of the cells around defects was characterized as follows. First, for each defect, we rotated the confocal image horizontally so that the defect arm was orientated in the positive direction of the x -axis. For $-1/2$ defects, we did this rotation for each of their three arms and obtained a set of three images from each defect. Then, for each rotated confocal image $I(\mathbf{r})$, where \mathbf{r} is the coordinate relative to the defect, we obtained the three-dimensional cell orientation $\mathbf{n}(\mathbf{r})$ by the three-dimensional version of the structure tensor method. For each pixel $\mathbf{r} = (x, y, z)$, which was chosen from the plane corresponding to the bottom layer in each region, we calculated the three-dimensional structure tensor:

$$J(\mathbf{r}) = \begin{pmatrix} [\Delta_x I, \Delta_x I]_{\mathbf{r}} & [\Delta_y I, \Delta_y I]_{\mathbf{r}} & [\Delta_z I, \Delta_x I]_{\mathbf{r}} \\ [\Delta_x I, \Delta_y I]_{\mathbf{r}} & [\Delta_y I, \Delta_y I]_{\mathbf{r}} & [\Delta_z I, \Delta_y I]_{\mathbf{r}} \\ [\Delta_x I, \Delta_z I]_{\mathbf{r}} & [\Delta_y I, \Delta_z I]_{\mathbf{r}} & [\Delta_z I, \Delta_z I]_{\mathbf{r}} \end{pmatrix}, \quad (7)$$

where $\Delta_x I \equiv I(x+1, y, z) - I(x-1, y, z)$, $\Delta_y I$ and $\Delta_z I$ are defined likewise, $[g, h]_{\mathbf{r}} \equiv \sum_{(x', y', z') \in \text{ROI}_{\mathbf{r}}^{\ell_x, \ell_y, \ell_z}} g(x', y', z') h(x', y', z') f_{\mathbf{r}}^{\sigma}(x', y', z')$. Here, the summation is taken over a three-dimensional region of interest $\text{ROI}_{\mathbf{r}}^{\ell_x, \ell_y, \ell_z}$, which is a cuboid of size $\ell_x \times \ell_y \times \ell_z$ centered at \mathbf{r} , with $\ell_x = \ell_y \approx 4.3 \mu\text{m}$ (24 pixels) and $\ell_z \approx 3.8 \mu\text{m}$ (24 pixels). The Gaussian kernel $f_{\mathbf{r}}^{\sigma}(x', y', z')$ is defined by $f_{\mathbf{r}}^{\sigma}(x', y', z') \equiv \exp[-\frac{(x'-x)^2 + (y'-y)^2 + (z'-z)^2}{2\sigma^2}]$ with $\sigma = 2.2 \mu\text{m}$. Then the three-dimensional cell orientation $\mathbf{n}_3(\mathbf{r})$ is given by the eigenvector of $J(\mathbf{r})$ associated with the smallest eigenvalue. The orientation $\mathbf{n}_3(\mathbf{r})$ is then represented by angles $\psi(\mathbf{r})$ and $\theta(\mathbf{r})$ such that $\mathbf{n}_3 = (\cos \theta \cos \psi, \cos \theta \sin \psi, \sin \theta)$ with $0 \leq \psi < 2\pi$ and $-\pi/2 \leq \theta < \pi/2$. As is clear from the definition, the angle $\psi(\mathbf{r})$ specifies the two-dimensional cell orientation

$\mathbf{n}(\mathbf{r})$ by $\mathbf{n} = (\cos \psi, \sin \psi)$ and $\theta(\mathbf{r})$ indicates the angle between the three-dimensional orientation and the xy -plane. Note that $\mathbf{n}_3(\mathbf{r})$ and $-\mathbf{n}_3(\mathbf{r})$ are equivalent, so that the sign of $\mathbf{n}(\mathbf{r})$ and $\theta(\mathbf{r})$ can be changed simultaneously.

To investigate statistical properties of the cell tilt angle around $\pm 1/2$ topological defects, we need to define tilt angles whose sign can be determined unambiguously. The simplest choice is to take the ensemble average of $|\theta(\mathbf{r})|$, which can be used to detect the presence of the three-dimensional tilting. We took this average over isolated defects of each sign, separated by a distance longer than $9 \mu\text{m}$ from the nearest defect, and this defines our $\theta_{\mathbf{n}}^{\pm}(\mathbf{r})$. To characterize the polar order, we need an angle that can take both positive and negative values. Here we chose such a sign that the tilt angle is positive if the cell end farther from the defect is lifted above the substrate. More specifically, we defined the reference director field $\mathbf{n}_{\text{ref}}^{\pm} \equiv (\cos(\pm\phi/2), \sin(\pm\phi/2))$ for $\pm 1/2$ defects, with the azimuth ϕ of the position \mathbf{r} in the xy -plane, and took the average of the field $\theta(\mathbf{r}) \text{sign}[\mathbf{n}_{\text{ref}}^{\pm} \cdot \mathbf{n}(\mathbf{r})]$ over isolated defects (with the same criterion on the distance from other defects). This is our $\theta_{\mathbf{p}}^{\pm}(\mathbf{r})$ which characterized the polar order. The polarity-induced force is then $\mathbf{f}_{\mathbf{p}}^{\pm}(\mathbf{r}) \propto \theta_{\mathbf{p}}^{\pm}(\mathbf{r}) \mathbf{n} \text{sign}[\mathbf{n}_{\text{ref}}^{\pm} \cdot \mathbf{n}(\mathbf{r})]$. In Supplementary Fig. 4d, we show its radial component $f_{\mathbf{p},r}^{\pm}$, which is proportional to $\theta_{\mathbf{p}}^{\pm}(\mathbf{r}) |\cos[\phi - \psi(\mathbf{r})]|$.

Theoretical calculations

To theoretically account for the experimental result of the mean radial velocity $\bar{v}_r^{\pm}(r)$, in particular the influx toward $-1/2$ defects shown in Fig. 2e,f, we solved the force balance equations (1) and (2). While detailed descriptions on the solutions are given in Supplementary Information, here we outline the theoretical assumptions and the methods to obtain the theoretical results shown in Fig. 4a, which satisfactorily reproduced the experimental data when the influx toward $-1/2$ defects was strongest.

First we assume the director field winding uniformly around a $+1/2$ or $-1/2$ defect, $\mathbf{n}^{\pm}(r, \phi) = (\cos(\pm\phi/2), \sin(\pm\phi/2))$, where (r, ϕ) is the two-dimensional polar coordinate, centered at the defect core. The nematic order tensor $\mathbf{Q}^{\pm}(r, \phi)$ is then given by

$$\mathbf{Q}^{\pm}(r, \phi) = S(r) \begin{pmatrix} \cos(\pm\phi) & \sin(\pm\phi) \\ \sin(\pm\phi) & -\cos(\pm\phi) \end{pmatrix}, \quad (8)$$

with the scalar nematic order parameter $S(r)$ left as a free parameter. Based on the assumption that \mathbf{Q}^{\pm} minimizes the nematic free energy, $S(r)$ can be theoretically

expressed by the following Padé approximant [9, 34, 35]:

$$S(r) = S_0 F(r/r_S), \quad F(x) \approx x \sqrt{\frac{0.34 + 0.07x^2}{1 + 0.41x^2 + 0.07x^4}}, \quad (9)$$

with the defect core radius r_S and $S_0 = S(\infty)$. To determine the value of r_S , we fitted Eq. (9) to the experimental data of the coherency $C(r)$ (Supplementary Fig. 5a,b) and obtained $r_S = 1.2 \mu\text{m}$. Note that, because the angle field $\psi(\mathbf{r})$ does not contain information of the defect core, the nematic order parameter evaluated by Eq. (5) is not suitable for estimating r_S . Concerning S_0 , it always appears as a product with either ϵ or a_n , so that we fix $S_0 = 1$ without loss of generality.

The case without three-dimensional cell tilting, described by Eq. (1), was already dealt with by earlier studies [9, 20]. Since Eq. (1) is linear, we can readily solve it and obtain, for the mean radial velocity,

$$\bar{v}_r^\pm(r) = -\epsilon \frac{a_n}{\xi_0} S(r) \frac{S'(r) \pm S(r)/r}{1 - \epsilon^2 S(r)^2}. \quad (10)$$

Then we can show, with Eq. (9), that it is negative for $+1/2$ defects and positive for $-1/2$ defects, for all $r > 0$ (see Supplementary Information, Sec. I). In Fig. 4a inset, by the dotted lines, we showed $\bar{v}_r^\pm(r)$ for $\epsilon = 0.25$, $a_n/\xi_0 = 0.055 \mu\text{m}^2/\text{min}$, $r_S = 1.2 \mu\text{m}$.

In fact, even in the presence of three-dimensional cell tilting and polar order, i.e., in the case of Eq. (2), it is linear in \mathbf{v} and the solution for the case of $\pm 1/2$ defects is given by

$$\mathbf{v}^\pm(r, \phi) = \xi_0^{-1} (\mathbf{1} - \epsilon_0 \cos \theta_n^\pm(r, \phi) \mathbf{Q}^\pm)^{-1} [\nabla \cdot (-a_n^0 \cos \theta_n^\pm(r, \phi) \mathbf{Q}^\pm) + a_p^0 \theta_p^\pm(r, \phi) \mathbf{n}^\pm]. \quad (11)$$

Regarding the first term that describes the contribution by non-uniform nematic tilting, we determined $\theta_n^\pm(r, \phi)$ by time-lapse and end-point confocal observations. Because we could not obtain clear spatial profile of $\theta_n^\pm(r, \phi)$ from the time-lapse observation due to photobleaching, we used high-quality, end-point confocal images to determine the spatial profile, then calibrated its amplitude by the time-lapse observation to account for the time period of interest. First, on the spatial profile, our end-point confocal observation (Fig. 4b and Supplementary Fig. 4e,f) suggests that $\theta_n^\pm(r, \phi) = \theta_n^\infty + (\theta_n^0 - \theta_n^\infty) \exp(-r^2/r_\theta^2)$ with constants θ_n^∞ , θ_n^0 , r_θ , regardless of ϕ and the sign of the defect. From the spatial profile, we obtained $r_\theta = 1 \mu\text{m}$. For the peak height, we used time-lapse observations for $200 \text{ min} \leq t \leq 250 \text{ min}$, during which the influx toward $-1/2$ defects was strongest for this strain (Supplementary Fig. 6a), and estimated $\theta_n^\infty = 0.2$ and $\theta_n^0 = 0.25$ (Supplementary Fig. 6b).

To see the influence of the nematic tilting, we numerically calculated $\bar{v}_r^\pm(r)$ with $\theta_n^\infty = 0.3$ and $\theta_n^0 = 0.75$, which were estimated from the end-point confocal observation, without polar order (Fig. 4a inset, the solid

line). The other parameters were $\epsilon_0 = 0.25$, $a_n/\xi_0 = 0.055 \mu\text{m}^2/\text{min}$ and $r_S = 1.2 \mu\text{m}$. The strength of the influx toward $-1/2$ defects obtained thereby was smaller than the experimental result, indicating that the nematic tilting is insufficient to quantitatively explain the influx toward $-1/2$ defects.

For the polar contribution to Eq. (11), we determined the spatial structure of $\theta_p^\pm(r, \phi)$ by the end-point confocal observation (Supplementary Fig. 5g,h, shown in the form of $f_{p,r}^\pm \propto \theta_p^\pm(r, \phi) |\cos[\phi - \psi(r, \phi)]|$). Then we calibrated the amplitude by multiplying the ratio of $\langle \theta_p^\pm \rangle_{0 < x < 10 \mu\text{m}, y=0}$ from the time-lapse observation for $200 \text{ min} \leq t \leq 250 \text{ min}$ (Supplementary Fig. 6c) to that from the end-point observation (Fig. 4d).

We are finally left to determine the following parameters: ϵ_0 , a_n^0/ξ_0 , and a_p^0/ξ_0 . First, we found that the friction anisotropy ϵ hardly changed the structure of the velocity field (data not shown), so that we chose $\epsilon_0 = 0.25$. Then we tuned a_n^0/ξ_0 and a_p^0/ξ_0 to reproduce the experimental data of $\bar{v}_r^\pm(r)$ and obtained $a_n^0/\xi_0 = 0.055 \mu\text{m}^2/\text{min}$ and $a_p^0/\xi_0 = 0.8 \mu\text{m}/\text{min}$, with the results shown in Fig. 4a.

ACKNOWLEDGMENTS

We are grateful to S. Ramaswamy for motivating us to investigate polar order in three-dimensional orientations. We thank Y. T. Maeda and H. Salman for sharing the plasmid DNA pZA3R-EYFP and K. Inoue for producing the strain MG1655-pZA3R-EYFP. We also acknowledge discussions with K. Kawaguchi, D. Nishiguchi, M. Sano, and Y. Zushi. This work is supported by KAKENHI from Japan Society for the Promotion of Science (JSPS) (No. 19H05800, 20H00128), by KAKENHI for JSPS Fellows (No. 20J10682), and by JST, PRESTO Grant No. JPMJPR18L6, Japan.

COMPETING INTERESTS

The authors declare no competing interests.

AUTHOR CONTRIBUTIONS

T.S. and K.A.T. designed research. T.S. performed all bacterial experiments and analyzed data. T.S. and K.A.T. did the modeling, and T.S. wrote the codes for the numerical calculations. T.S. performed the theoretical calculations. T.S. and K.A.T. wrote the manuscript.

DATA AVAILABILITY

The data that support the findings of this study are available from the corresponding author upon reasonable request.

CODE AVAILABILITY

The codes used in this study are available from the corresponding author upon reasonable request.

* t.shimaya@noneq.phys.s.u-tokyo.ac.jp

† kat@kaztake.org

- [1] H. Flemming, J. Wingender, U. Szewzyk, P. Steinberg, S. A. Rice, and S. Kjelleberg, “Biofilms: an emergent form of bacterial life,” *Nat. Rev. Microbiol.* **14**, 563–575 (2016).
- [2] P. Su, C. Liao, J. Roan, S. Wang, A. Chiou, and W. Syu, “Bacterial colony from two-dimensional division to three-dimensional development,” *PLOS ONE* **7**, 1–10 (2012).
- [3] M. A. A. Grant, B. Waclaw, R. J. Allen, and P. Cicuta, “The role of mechanical forces in the planar-to-bulk transition in growing *Escherichia coli* microcolonies,” *J. R. Soc. Interface* **11**, 20140400 (2014).
- [4] M. Duvernoy, T. Mora, M. Ardré, V. Croquette, D. Bensimon, C. Quilliet, J. Ghigo, M. Balland, C. Beloin, S. Lecuyer, and N. Desprat, “Asymmetric adhesion of rod-shaped bacteria controls microcolony morphogenesis,” *Nat. Commun.* **9** (2018), 10.1038/s41467-018-03446-y.
- [5] F. Beroz, J. Yan, Y. Meir, B. Sabass, H. A. Stone, B. L. Bassler, and N. S. Wingreen, “Verticalization of bacterial biofilms,” *Nat. Phys.* **14**, 954–960 (2018).
- [6] Z. You, D. J. G. Pearce, A. Sengupta, and L. Giomi, “Mono- to multilayer transition in growing bacterial colonies,” *Phys. Rev. Lett.* **123**, 178001 (2019).
- [7] R. Hartmann, P. K. Singh, P. Pearce, R. Mok, B. Song, F. Díaz-Pascual, J. Dunkel, and K. Drescher, “Emergence of three-dimensional order and structure in growing biofilms,” *Nat. Phys.* **15**, 251–256 (2019).
- [8] S. C. Takatori and K. K. Mandadapu, “Motility-induced buckling and glassy dynamics regulate three-dimensional transitions of bacterial monolayers,” arXiv:2003.05618 .
- [9] K. Copenhagen, R. Alert, N. S. Wingreen, and J. W. Shaevitz, “Topological defects promote layer formation in *Myxococcus xanthus* colonies,” *Nat. Phys.* **17**, 211–215 (2021).
- [10] Z. You, D. J. G. Pearce, A. Sengupta, and L. Giomi, “Geometry and mechanics of microdomains in growing bacterial colonies,” *Phys. Rev. X* **8**, 031065 (2018).
- [11] D. Dell’Arciprete, M. L. Blow, A. T. Brown, F. D. C. Farrell, J. S. Lintuvuori, A. F. McVey, D. Marenduzzo, and W. C. K. Poon, “A growing bacterial colony in two dimensions as an active nematic,” *Nat. Commun.* **9** (2018), 10.1038/s41467-018-06370-3.
- [12] A. Doostmohammadi, S. P. Thampi, and J. M. Yeomans, “Defect-mediated morphologies in growing cell colonies,” *Phys. Rev. Lett.* **117**, 048102 (2016).
- [13] A. Sengupta, “Microbial active matter: A topological framework,” *Front. Phys.* **8**, 184 (2020).
- [14] C. Peng, T. Turiv, Y. Guo, Q. Wei, and O. D. Lavrentovich, “Command of active matter by topological defects and patterns,” *Science* **354**, 882–885 (2016).
- [15] M. M. Genkin, A. Sokolov, O. D. Lavrentovich, and I. S. Aranson, “Topological defects in a living nematic ensnare swimming bacteria,” *Phys. Rev. X* **7**, 011029 (2017).
- [16] T. B. Saw, W. Xi, B. Ladoux, and C. T. Lim, “Biological tissues as active nematic liquid crystals,” *Adv. Mater.* **30**, 1802579 (2018).
- [17] Y. I. Yaman, E. Demir, R. Vetter, and A. Kocabas, “Emergence of active nematics in chaining bacterial biofilms,” *Nat. Commun.* **10** (2019), 10.1038/s41467-019-10311-z.
- [18] O. J. Meacock, A. Doostmohammadi, K. R. Foster, Yeomans J. M., and W. M. Durham, “Bacteria solve the problem of crowding by moving slowly,” *Nat. Phys.* **17**, 205–210 (2021).
- [19] T. B. Saw, A. Doostmohammadi, V. Nier, L. Kocgozlu, S. Thampi, Y. Toyama, P. Marcq, C. T. Lim, J. M. Yeomans, and B. Ladoux, “Topological defects in epithelia govern cell death and extrusion,” *Nature* **544**, 212–216 (2017).
- [20] K. Kawaguchi, R. Kageyama, and M. Sano, “Topological defects control collective dynamics in neural progenitor cell cultures,” *Nature* **545**, 327–331 (2017).
- [21] G. Duclos, C. Erlenkämper, J. Joanny, and P. Silberzan, “Topological defects in confined populations of spindle-shaped cells,” *Nat. Phys.* **13**, 58–62 (2017).
- [22] T. Turiv, J. Krieger, G. Babakhanova, H. Yu, S. V. Shiyankovskii, Q. Wei, M. Kim, and O. D. Lavrentovich, “Topology control of human fibroblast cells monolayer by liquid crystal elastomer,” *Sci. Adv.* **6** (2020), 10.1126/sciadv.aaz6485.
- [23] Y. Maroudas-Sacks, L. Garion, L. Shani-Zerbib, A. Livshits, E. Braun, and K. Keren, “Topological defects in the nematic order of actin fibres as organization centres of *Hydra* morphogenesis,” *Nat. Phys.* **17**, 251–259 (2021).
- [24] F. D. C. Farrell, O. Hallatschek, D. Marenduzzo, and B. Waclaw, “Mechanically driven growth of quasi-two-dimensional microbial colonies,” *Phys. Rev. Lett.* **111**, 168101 (2013).
- [25] M. R. Warren, H. Sun, Y. Yan, J. Cremer, B. Li, and T. Hwa, “Spatiotemporal establishment of dense bacterial colonies growing on hard agar,” *eLife* **8**, e41093 (2019).
- [26] D. Volfson, S. Cookson, J. Hasty, and L. S. Tsimring, “Biomechanical ordering of dense cell populations,” *Proc. Natl. Acad. Sci. USA* **105**, 15346–15351 (2008).
- [27] D. Boyer, W. Mather, O. Mondragón-Palmino, S. Orozco-Fuentes, T. Danino, J. Hasty, and L. S. Tsimring, “Buckling instability in ordered bacterial colonies,” *Phys. Biol.* **8**, 026008 (2011).
- [28] D. van Holthe tot Echten, G. Nordemann, M. Wehrens, S. Tans, and T. Idema, “Defect dynamics in growing bacterial colonies,” arXiv:2003.10509 .
- [29] A. Doostmohammadi, J. Ignés-Mullol, J. M. Yeomans, and F. Sagués, “Active nematics,” *Nat. Commun.* **9** (2018), 10.1038/s41467-018-05666-8.
- [30] M. Doumic, S. Hecht, and D. Peurichard, “A purely mechanical model with asymmetric features for early morphogenesis of rod-shaped bacteria micro-colony,” *Math.*

- Biosci. Eng. **17**, 6873–6908 (2020).
- [31] D. L. Blair, T. Neicu, and A. Kudrolli, “Vortices in vibrated granular rods,” *Phys. Rev. E* **67**, 031303 (2003).
- [32] D. Volfson, A. Kudrolli, and L. S. Tsimring, “Anisotropy-driven dynamics in vibrated granular rods,” *Phys. Rev. E* **70**, 051312 (2004).
- [33] J. K. Sveen, “An introduction to MatPIV 1.6.1,” (2004), eprint no. 2, ISSN 0809-4403, Dept. of Mathematics, University of Oslo.
- [34] L. M. Pismen, *Patterns and interfaces in dissipative dynamics* (Springer, 2006).
- [35] L. M. Pismen, *Vortices in Nonlinear Fields. From Liquid Crystals to Superfluids. From Non-Equilibrium Patterns to Cosmic Strings* (Oxford University Press, 1999).

Supplementary Information for “3D-induced polar order and topological defects in growing bacterial populations”

Takuro Shimaya* and Kazumasa A. Takeuchi†
Department of Physics, The University of Tokyo,
7-3-1 Hongo, Bunkyo-ku, Tokyo, 113-0033, Japan.

I. MEAN RADIAL VELOCITY WITHOUT CELL TILTING AND PROLIFERATION

Here we derive the analytical solution of the mean radial velocity $\bar{v}_r^\pm(r)$ for the case without three-dimensional tilting of the cells and cell proliferation. This case is described by Eq. (1), which reads

$$\boldsymbol{\xi} \mathbf{v} = \nabla \cdot (-a_n \mathbf{Q}), \quad (\text{S1})$$

where the friction tensor is $\boldsymbol{\xi} = \xi_0(\mathbf{1} - \epsilon \mathbf{Q})$ with the friction anisotropy ϵ ($0 < \epsilon < 1$). Around a $\pm 1/2$ defect, we assume the simplest director field

$$\mathbf{n}^\pm(r, \phi) = \begin{pmatrix} \cos(\pm\phi/2) \\ \sin(\pm\phi/2) \end{pmatrix}, \quad (\text{S2})$$

where (r, ϕ) is the two-dimensional polar coordinate centered at the defect core. Consequently, the nematic order tensor $\mathbf{Q}^\pm(\mathbf{r})$ is given by

$$\mathbf{Q}^\pm(r, \phi) = S(r) \begin{pmatrix} \cos(\pm\phi) & \sin(\pm\phi) \\ \sin(\pm\phi) & -\cos(\pm\phi) \end{pmatrix}, \quad (\text{S3})$$

with a function $S(r)$, which is the scalar nematic order parameter. Under the assumption that the active stress coefficient a_n is constant, following the previous works [1, 2], we obtain the velocity $\mathbf{v}^\pm(r, \phi)$ as follows:

$$\mathbf{v}^+(r, \phi) = -\frac{a_n}{\xi_0} G^+(r) \begin{bmatrix} 1 \\ 0 \end{bmatrix} + \epsilon S(r) \begin{pmatrix} \cos \phi \\ \sin \phi \end{pmatrix}, \quad (\text{S4})$$

$$\mathbf{v}^-(r, \phi) = -\frac{a_n}{\xi_0} G^-(r) \begin{bmatrix} \cos 2\phi \\ -\sin 2\phi \end{bmatrix} + \epsilon S(r) \begin{pmatrix} \cos \phi \\ \sin \phi \end{pmatrix}, \quad (\text{S5})$$

with

$$G^\pm(r) = \frac{S'(r) \pm S(r)/r}{1 - \epsilon^2 S(r)^2}, \quad (\text{S6})$$

where $S'(r) = \frac{dS}{dr}$. Then the mean radial velocity $\bar{v}_r^\pm(r)$ can be calculated as

$$\bar{v}_r^\pm(r) = \frac{1}{2\pi} \int_0^{2\pi} d\phi \begin{pmatrix} \cos \phi \\ \sin \phi \end{pmatrix} \cdot \mathbf{v}^\pm(r, \phi) = -\epsilon \frac{a_n}{\xi_0} S(r) \frac{S'(r) \pm S(r)/r}{1 - \epsilon^2 S(r)^2}. \quad (\text{S7})$$

Since the parameters satisfy $a_n > 0$, $\xi_0 > 0$, $0 < \epsilon < 1$, and $0 \leq S \leq 1$, the direction of the mean radial velocity around the defect is determined by $\text{sign}[-(S'(r) \pm S(r)/r)]$.

To proceed, we need to determine $S(r)$. Here we use the following Padé approximant due to earlier studies [2–4], obtained by assuming that $\mathbf{Q}^\pm(r, \phi)$ minimizes the nematic free energy:

$$S(r) = S_0 F(r/r_S), \quad F(x) \simeq x \sqrt{\frac{0.34 + 0.07x^2}{1 + 0.41x^2 + 0.07x^4}}, \quad (\text{S8})$$

with the defect core radius r_S and $S_0 = S(\infty)$. Then, $\text{sign}[\bar{v}_r^\pm(r)] = -\text{sign}[S'(r) \pm S(r)/r] = -\text{sign}[F'(x) \pm F(x)/x]$ and we can show that it is negative for $+1/2$ defects and positive for $-1/2$ defects, for all $r > 0$, as previously known. In Fig. 4a inset, by the dotted lines, we showed $\bar{v}_r^\pm(r)$ for $\epsilon S_0 = 0.25$, $a_n S_0 / \xi_0 = 0.055 \mu\text{m}^2/\text{min}$, $r_S = 1.2 \mu\text{m}$.

* t.shimaya@noneq.phys.s.u-tokyo.ac.jp

† kat@kaztake.org

II. THEORY WITH CELL PROLIFERATION

Here we show that cell proliferation does not change the direction of the mean radial velocity around defects. Following ref.[5], we start from the following hydrodynamic equations:

$$\frac{D\rho}{Dt} = \lambda\rho + \mathcal{D}\nabla^2\rho, \quad (\text{S9})$$

$$\frac{D(\rho\mathbf{v})}{Dt} = \nabla \cdot \boldsymbol{\sigma} - \boldsymbol{\xi}\mathbf{v}, \quad (\text{S10})$$

with the material derivative $D/Dt = \partial_t + \mathbf{v} \cdot \nabla + (\nabla \cdot \mathbf{v})$, the cell density ρ , the proliferation (growth) rate λ and the diffusion constant \mathcal{D} . The material derivative of the momentum density $\rho\mathbf{v}$ can be expressed as

$$\begin{aligned} \frac{D(\rho\mathbf{v})}{Dt} &= \frac{\partial(\rho\mathbf{v})}{\partial t} + (\mathbf{v} \cdot \nabla)(\rho\mathbf{v}) + (\nabla \cdot \mathbf{v})\rho\mathbf{v} \\ &= \rho \frac{\partial\mathbf{v}}{\partial t} + \mathbf{v} \frac{\partial\rho}{\partial t} + \rho(\mathbf{v} \cdot \nabla)\mathbf{v} + \mathbf{v}(\mathbf{v} \cdot \nabla)\rho + (\nabla \cdot \mathbf{v})\rho\mathbf{v} \\ &= \rho \frac{\partial\mathbf{v}}{\partial t} + \rho(\mathbf{v} \cdot \nabla)\mathbf{v} + \mathbf{v} \frac{D\rho}{Dt}. \end{aligned} \quad (\text{S11})$$

In the overdamped and low Reynolds number limit, the first and second terms in the right-hand side can be neglected. Combining with Eqs. (S9) and (S10), we obtain

$$\mathbf{v}(\lambda\rho + \mathcal{D}\nabla^2\rho) = \nabla \cdot \boldsymbol{\sigma} - \boldsymbol{\xi}\mathbf{v}. \quad (\text{S12})$$

Assuming that the diffusion of the density is weak compared to the cell growth, Eq. (S12) can be rewritten as

$$\lambda\rho\mathbf{v} = \nabla \cdot \boldsymbol{\sigma} - \boldsymbol{\xi}\mathbf{v}. \quad (\text{S13})$$

With the active stress field $\boldsymbol{\sigma} = -a_n\mathbf{Q}$ and the friction $\boldsymbol{\xi} = \xi_0(\mathbf{1} - \epsilon\mathbf{Q})$, we obtain the following equation for the velocity field $\mathbf{v}^\pm(r, \phi)$ around a $\pm 1/2$ topological defect:

$$\mathbf{v} = [(\xi_0 + \lambda\rho)\mathbf{1} - \epsilon\xi_0\mathbf{Q}]^{-1}\nabla \cdot (-a_n\mathbf{Q}). \quad (\text{S14})$$

Assuming that a_n is constant, and using Eq. (S3) for the nematic order tensor, we obtain the following expression for the velocity field $\mathbf{v}^\pm(r, \phi)$ around a $\pm 1/2$ topological defect:

$$\mathbf{v}^+(r, \phi) = -\frac{a_n}{\xi_0}H^+(r) \left[(1 + \lambda\rho/\xi_0) \begin{pmatrix} 1 \\ 0 \end{pmatrix} + \epsilon S(r) \begin{pmatrix} \cos \phi \\ \sin \phi \end{pmatrix} \right] \quad (\text{S15})$$

$$\mathbf{v}^-(r, \phi) = -\frac{a_n}{\xi_0}H^-(r) \left[(1 + \lambda\rho/\xi_0) \begin{pmatrix} \cos 2\phi \\ -\sin 2\phi \end{pmatrix} + \epsilon S(r) \begin{pmatrix} \cos \phi \\ \sin \phi \end{pmatrix} \right] \quad (\text{S16})$$

with

$$H^\pm(r) = \frac{S'(r) \pm S(r)/r}{(1 + \lambda\rho/\xi_0)^2 - \epsilon^2 S(r)^2}. \quad (\text{S17})$$

Then we obtain the mean radial velocity \bar{v}_r^\pm as follows:

$$\bar{v}_r^\pm(r) = \frac{1}{2\pi} \int_0^{2\pi} d\phi \begin{pmatrix} \cos \phi \\ \sin \phi \end{pmatrix} \cdot \mathbf{v}^\pm(r, \phi) = -\epsilon \frac{a_n}{\xi_0} S(r) \frac{S'(r) \pm S(r)/r}{(1 + \lambda\rho/\xi_0)^2 - \epsilon^2 S(r)^2}. \quad (\text{S18})$$

Comparing with Eq. (S7), Eq. (S18) changed the denominator only, which is still positive because $\lambda, \rho > 0$. Therefore, the direction of the mean radial velocity is still determined by $\text{sign}[-(S'(r) \pm S(r)/r)]$ and the cell proliferation cannot change the direction of the mean radial velocity.

III. THEORY WITH NON-UNIFORM NEMATIC TILTING

Here we show that non-uniform nematic tilting, i.e., non-uniform $\theta_n(r, \phi)$, can realize the influx toward $-1/2$ defects without the 3D-induced polar order. Assuming $a_n(r, \phi) = a_n^0 \cos \theta_n(r, \phi)$, we have the following force balance equation:

$$\xi_0(\mathbf{1} - \epsilon_0 \cos \theta_n \mathbf{Q})\mathbf{v} = \nabla \cdot (-a_n^0 \cos \theta_n \mathbf{Q}). \quad (\text{S19})$$

Concerning the functional form of $\theta_n(r, \phi)$, our experimental data around $\pm 1/2$ defects (Fig. 4b and Supplementary Fig. 4e,f) suggest that it hardly depends on ϕ and the sign of the defect, i.e., $\theta_n^\pm(r, \phi) = \theta_n(r)$, and

$$\theta_n(r) = \theta_n^\infty + (\theta_n^0 - \theta_n^\infty) \exp(-r^2/r_\theta^2), \quad (\text{S20})$$

with constants $\theta_n^\infty, \theta_n^0 (> \theta_n^\infty), r_\theta$. From this, one can intuitively see that the active stress coefficient $a_n(r, \phi) = a_n^0 \cos \theta_n(r, \phi)$ becomes smaller near the defect core, which may generate a force toward the defect.

In the following, we analytically show the emergence of the influx toward $-1/2$ defects, due to the non-uniform $\theta_n(r)$ given by Eq. (S20). First, we can rewrite Eq. (S19) as

$$\xi_0(\mathbf{1} - \epsilon_0 \tilde{\mathbf{Q}}^\pm) \mathbf{v}^\pm = \nabla \cdot (-a_n^0 \tilde{\mathbf{Q}}^\pm), \quad (\text{S21})$$

with

$$\tilde{\mathbf{Q}}^\pm(r, \phi) = \tilde{S}(r) \begin{pmatrix} \cos(\pm\phi) & \sin(\pm\phi) \\ \sin(\pm\phi) & -\cos(\pm\phi) \end{pmatrix}, \quad (\text{S22})$$

and $\tilde{S}(r) = S(r) \cos \theta_n(r)$. In other words, introducing the r -dependence to the active stress coefficient is equivalent to changing the scalar nematic order $S(r)$. Therefore, we obtain the mean radial velocity $\bar{v}_r^\pm(r)$ in the same form as Eq. (S7):

$$\bar{v}_r^\pm(r) = -\epsilon_0 \frac{a_n}{\xi_0} \tilde{S}(r) \frac{\tilde{S}'(r) \pm \tilde{S}(r)/r}{1 - \epsilon_0^2 \tilde{S}(r)^2}. \quad (\text{S23})$$

As we described in Sec. I, the sign of the mean radial velocity is determined by $\text{sign}[-(\tilde{S}'(r) \pm \tilde{S}(r)/r)]$, meaning that this direction is sensitive to the functional form of $\tilde{S}(r)$.

Now we evaluate the sign of the mean radial velocity $\bar{v}_r^-(r)$ for $-1/2$ defects. It is determined by $-(\tilde{S}'(r) - \tilde{S}(r)/r)$, where $\tilde{S}(r) = S(r) \cos \theta_n(r)$ with $S(r)$ given by Eq. (S8) and $\theta_n(r)$ by Eq. (S20). We first deal with the case without nematic tilting, i.e., $\theta_n(r) = 0$ and $\tilde{S}(r) = S(r)$. Using $x \equiv r/r_S$, we have $-[S'(r) \pm S(r)/r] = -(S_0/r_S)[F'(x) \pm F(x)/x]$, with $F(x)$ given by Eq. (S8) and

$$F'(x) \simeq \frac{0.34 + 0.14x^2 + 0.0049x^4}{(1 + 0.41x^2 + 0.07x^4)^2} \left(\frac{0.34 + 0.07x^2}{1 + 0.41x^2 + 0.07x^4} \right)^{-1/2}. \quad (\text{S24})$$

Therefore, for the $-1/2$ defects, we obtain

$$\begin{aligned} -\left(S'(r) - \frac{S(r)}{r} \right) &= -\frac{S_0}{r_S} \left(F'(x) - \frac{F(x)}{x} \right) \\ &\simeq \frac{S_0}{r_S} \frac{x^2(0.069 + 0.048x^2 + 0.0049x^4)}{(1 + 0.41x^2 + 0.07x^4)^2} \left(\frac{0.34 + 0.07x^2}{1 + 0.41x^2 + 0.07x^4} \right)^{-1/2}. \end{aligned} \quad (\text{S25})$$

In particular, near the defect core, $x \ll 1$, we have

$$-\left(S'(r) - \frac{S(r)}{r} \right) \simeq 0.12 \frac{S_0}{r_S} x^2 + \mathcal{O}(x^4) > 0. \quad \left(x = \frac{r}{r_S} \ll 1 \right) \quad (\text{S26})$$

Therefore, there arises outflux from $-1/2$ defects, as already known, in the case without nematic tilting.

In the presence of non-uniform nematic tilting, we replace $S(r)$ with $\tilde{S}(r) = S(r) \cos \theta_n(r)$. Since

$$-\left(\tilde{S}'(r) - \frac{\tilde{S}(r)}{r} \right) = -\left(S'(r) - \frac{S(r)}{r} \right) \cos \theta_n(r) + S(r) \theta_n'(r) \sin \theta_n(r) \quad (\text{S27})$$

and

$$\theta_n'(r) = -(\theta_n^0 - \theta_n^\infty) \frac{2r}{r_\theta^2} \exp(-r^2/r_\theta^2), \quad (\text{S28})$$

we have, for $r \ll r_S$ and $r \ll r_\theta$,

$$-\left(S'(r) - \frac{S(r)}{r} \right) \simeq 1.2 \frac{S_0}{r_S} \left[0.1 \cos \theta_n^0 \left(\frac{r}{r_S} \right)^2 - (\theta_n^0 - \theta_n^\infty) \sin \theta_n^0 \left(\frac{r}{r_\theta} \right)^2 \right]. \quad (\text{S29})$$

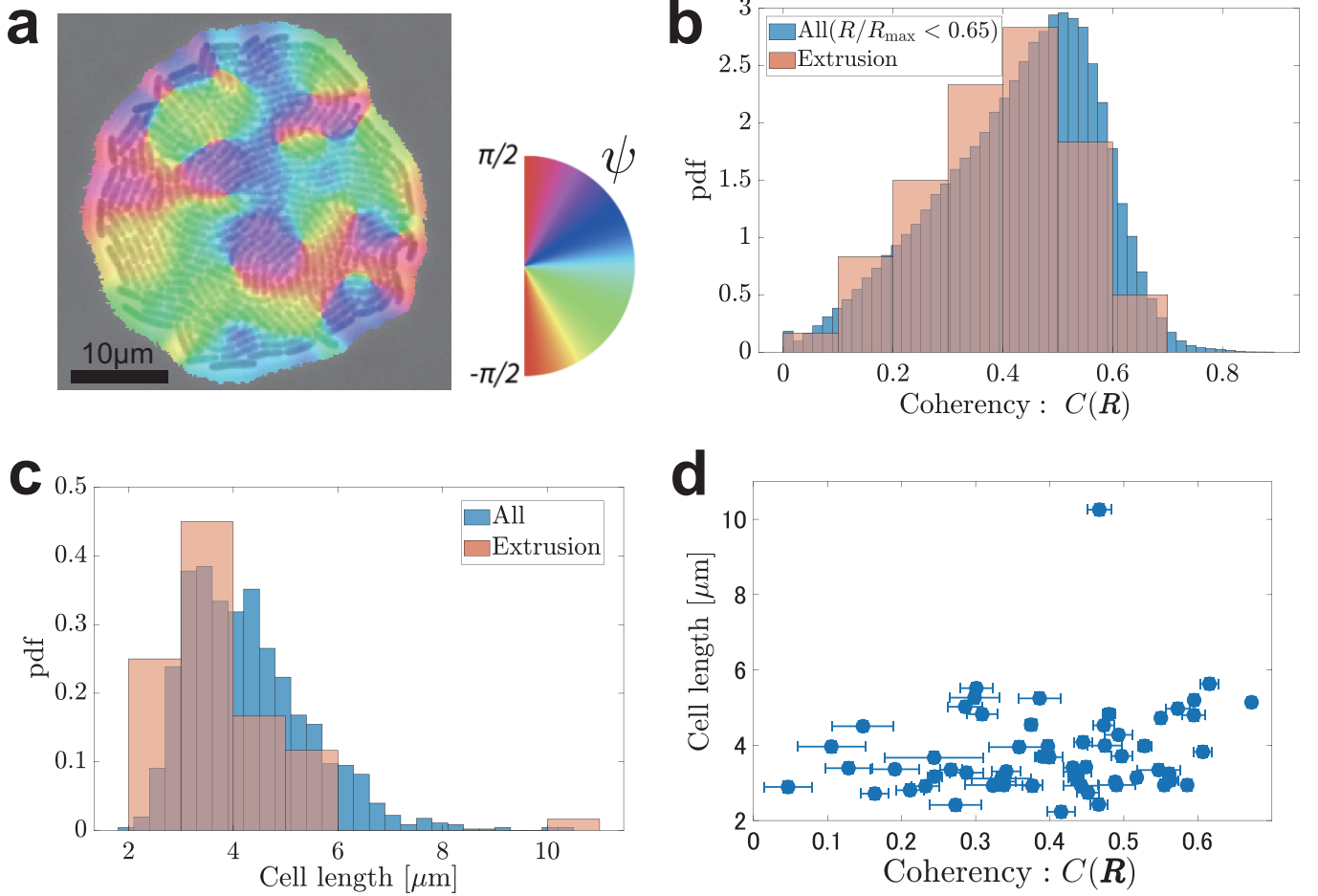
Therefore, its sign is determined by

$$\text{sign}[\bar{v}_r^-(r)] = \text{sign} \left[0.1 \frac{\cos \theta_n^0}{r_S^2} - (\theta_n^0 - \theta_n^\infty) \frac{\sin \theta_n^0}{r_\theta^2} \right]. \quad (r \ll r_S, r_\theta). \quad (\text{S30})$$

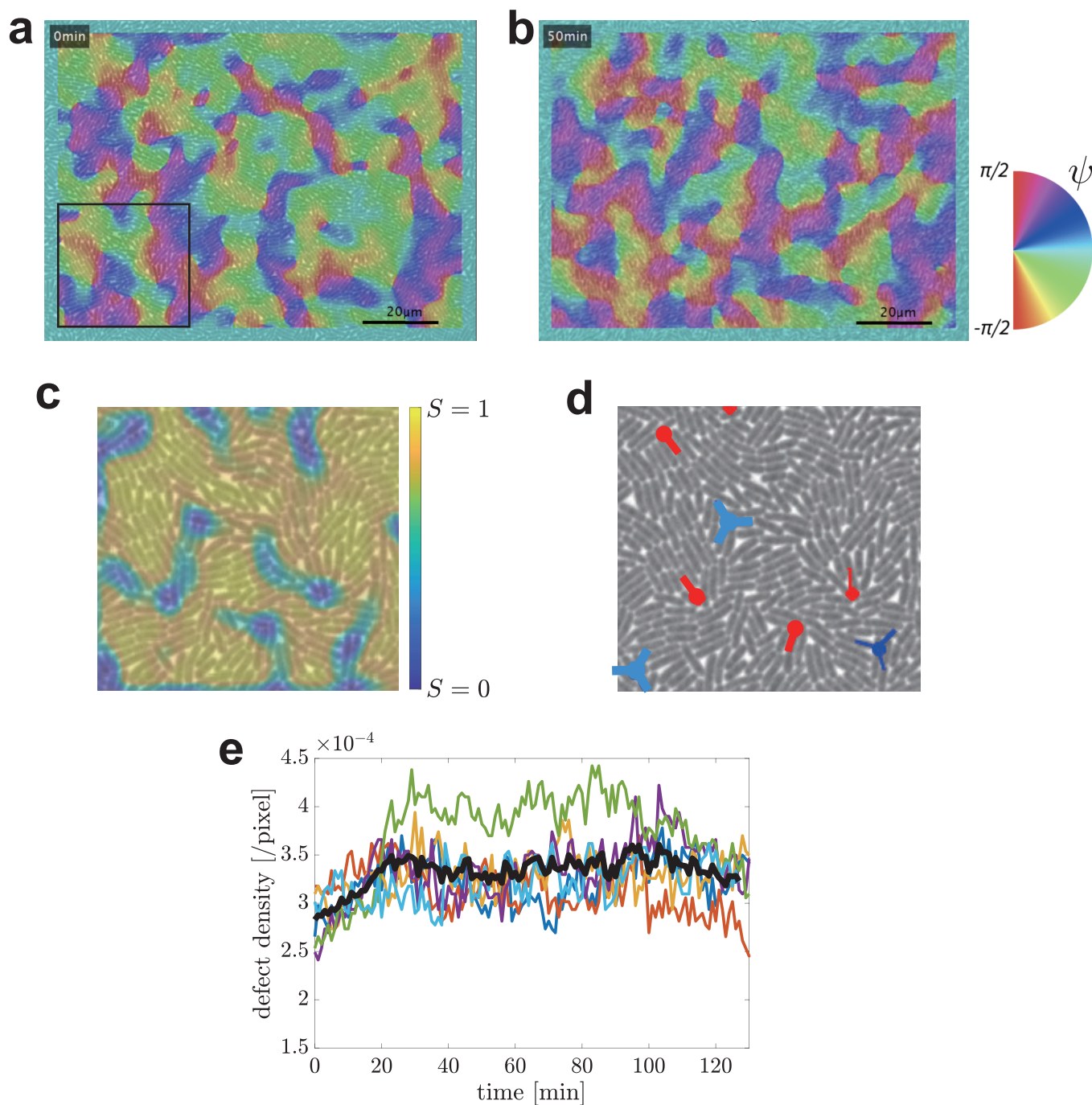
This result shows that the influx toward $-1/2$ defects appears if the peak of the tilt angle is sufficiently high or sharp, i.e., if $\theta_n^0 - \theta_n^\infty$ is sufficiently large or r_θ is sufficiently small. This is demonstrated by our numerical evaluation with $r_S = 1.2 \mu\text{m}$, $r_\theta = 1 \mu\text{m}$, $\theta_n^\infty = 0.3$ and for various θ_n^0 ($0.3 \leq \theta_n^0 \leq 1.5$), shown in Supplementary Fig. 5c, where $\bar{v}_r^-(r)$ starts to show a negative minimum when θ_n^0 becomes sufficiently large.

Note, however, that the maximum strength of the influx toward $-1/2$ defects that we could achieve by the theory presented in this section, within a reasonable range of parameter values, was significantly weaker than the experimental observation. For example, the result with $\theta_n^\infty = 0.3$ and $\theta_n^0 = 0.75$, which are comparable to the experimentally observed values in Fig. 4b, exhibits very little influx (Fig. 4a inset, a blue solid line). This gap is cleared by taking into account the 3D-induced polar order (see the main text and Methods).

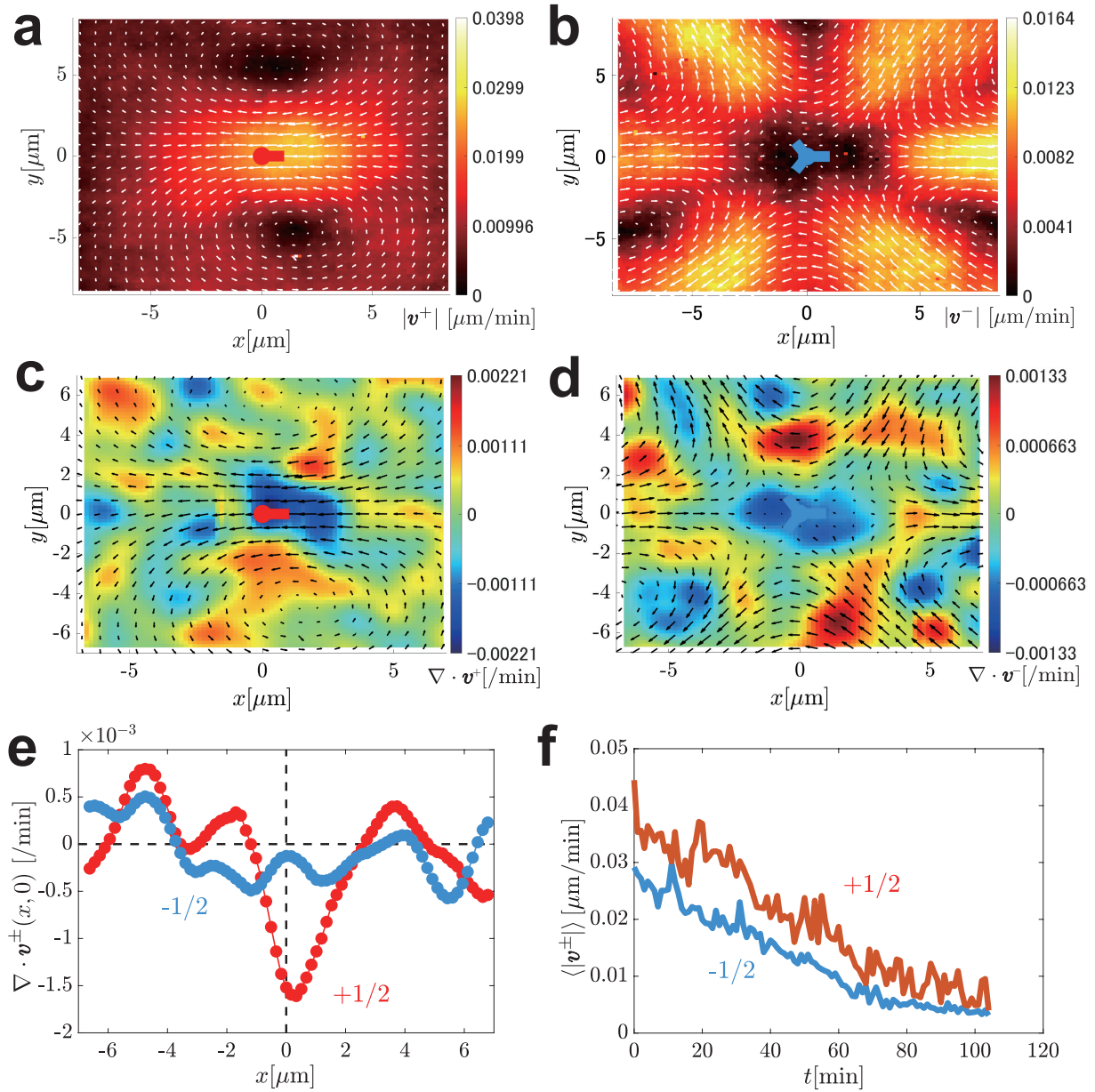
IV. SUPPLEMENTARY FIGURES



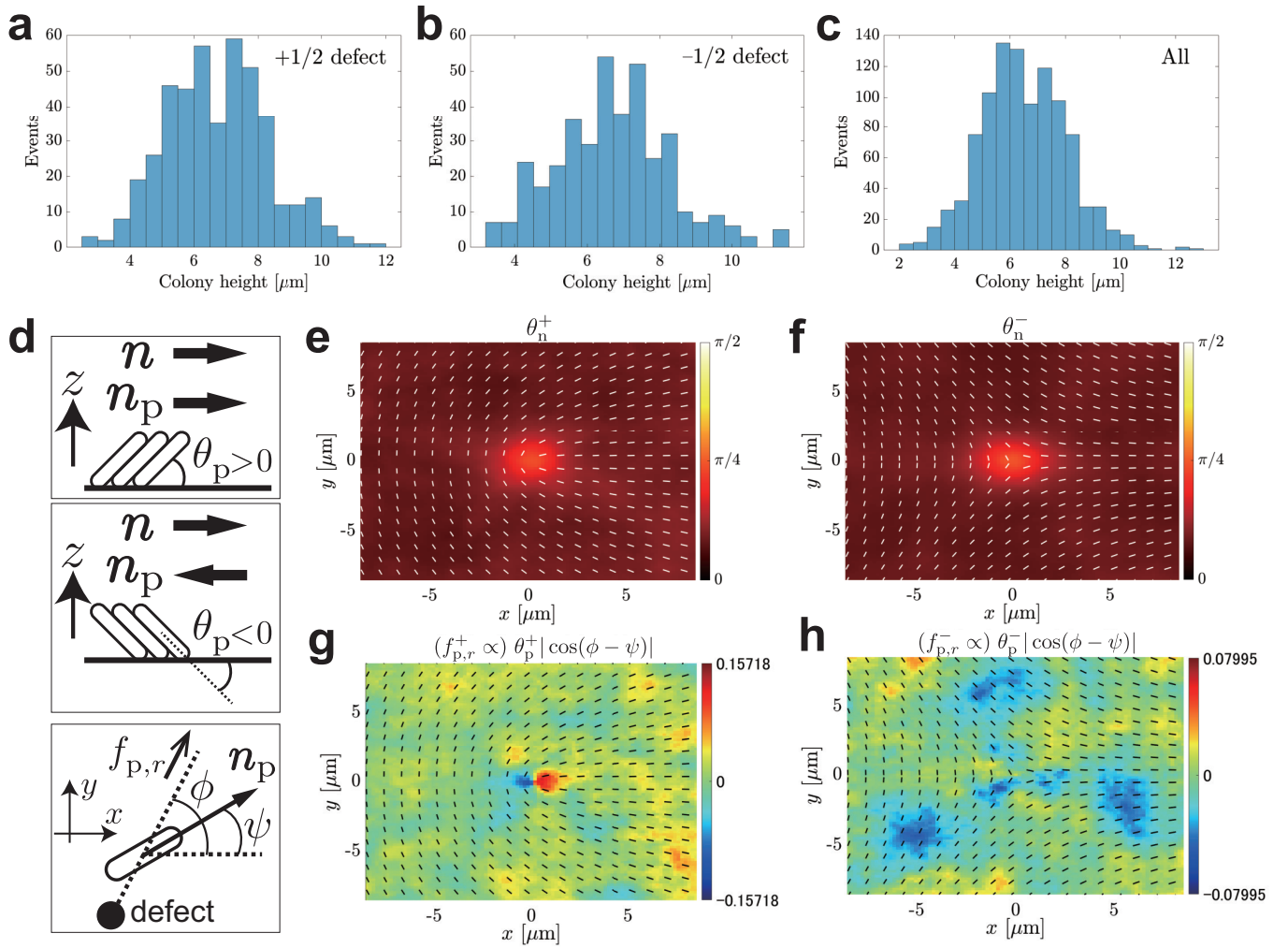
Supplementary Fig. 1. Supplemental results on circular colonies formed from a few cells. **a**, The cell orientation angle $\psi(\mathbf{R})$ obtained by the structure tensor method. **b**, Histogram of $C(\mathbf{R})$ for all cells in the region $R/R_{\max} < 0.65$ (blue, sample size $N = 1045164$) and that for the first extruded cells (red, sample size $N = 60$). **c**, Histogram of the cell length for all cells (blue, sample size $N = 1507$, collected from 6 independent colonies) and that for the first extruded cells (red, sample size $N = 60$). **d**, Scattered plot of the coherency $C(\mathbf{R})$ and the length of the first extruded cells. The horizontal error bars indicate the standard deviations of $C(\mathbf{R})$ in the pixels contained in the extruded cells. The vertical error bars, which indicate segmentation uncertainty in the image analysis ($\pm 0.15 \mu\text{m}$), are smaller than the symbol size.



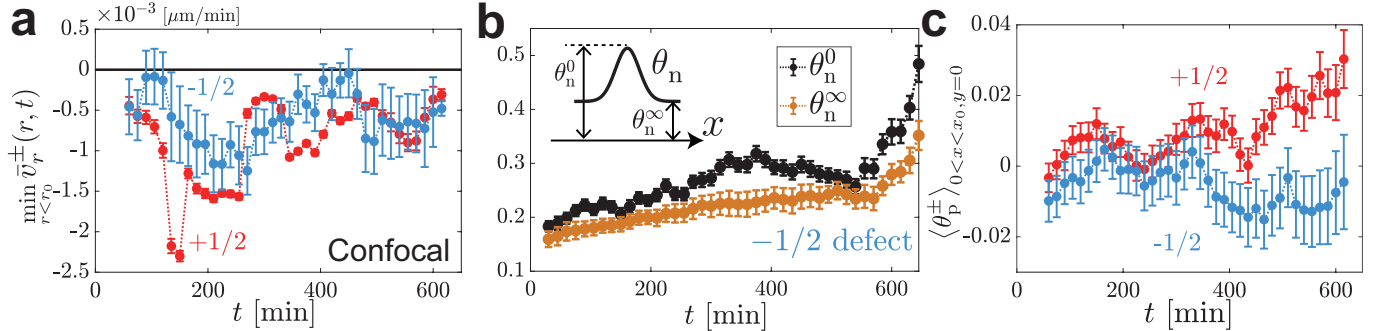
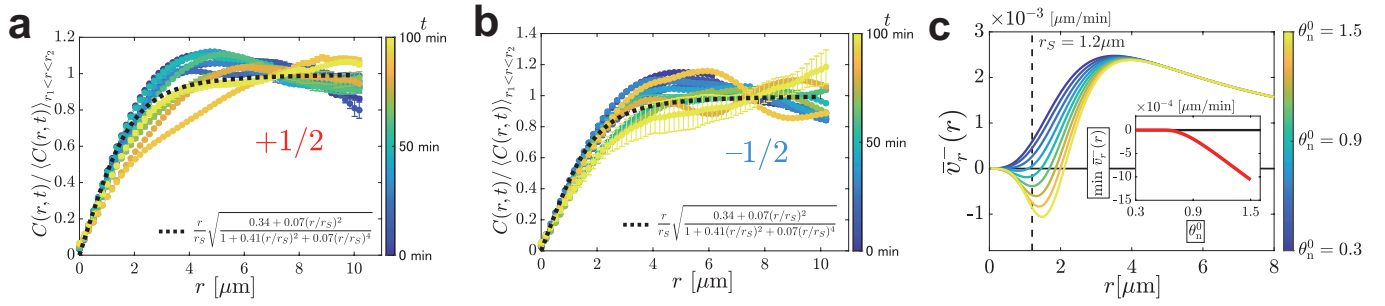
Supplementary Fig. 2. Cell orientation and topological defects in uniform colonies formed from numerous cells, observed by phase contrast microscopy. **a**, The cell orientation angle $\psi(\mathbf{R})$ at $t = 0$, when cells filled the bottom layer. **b**, The cell orientation angle $\psi(\mathbf{R})$ at $t = 50$ min after cells filled the bottom layer. **c**, The local nematic order parameter $S(\mathbf{R})$, for the region depicted by the black square in **(a)**, at $t = 0$. **d**, Topological defects, detected automatically from **(c)** at the local minima of $S(\mathbf{R})$. Red comets and blue trefoils indicate $+1/2$ and $-1/2$ defects, respectively. The arms of the symbols reflect the structure of the director field as illustrated in the insets of Fig. 2e,f. **e**, Time evolution of the number density of topological defects. Each colored line represents data from a single observation region, while the black bold line shows the ensemble average over 30 regions. The defect density increases until nearly $t = 30$ min.



Supplementary Fig. 3. Supplemental results on uniform colonies formed from numerous cells, observed by phase contrast microscopy. **a,b**, Velocity field $\mathbf{v}^\pm(\mathbf{r})$ (white arrows) and its norm (color map) around $+1/2$ defects (**a**) and $-1/2$ defects (**b**). We took the time average over $30 \text{ min} \leq t \leq 105 \text{ min}$, during which the defect density was constant (Supplementary Fig. 2e). **c,d**, Velocity field $\mathbf{v}^\pm(\mathbf{r})$ (black arrows) and its divergence (color map) around $+1/2$ defects (**c**) and $-1/2$ defects (**d**). These are identical to Fig. 2b,c but reprinted here for comparison. **e**, Divergence on the x-axis. **f**, Time evolution of the spatially averaged norm $\langle |\mathbf{v}^\pm(\mathbf{r})| \rangle$ around defects. The spatial average was taken in the region shown in (**a-d**).



Supplementary Fig. 4. Supplementary results on uniform colonies formed from numerous cells, obtained by end-point confocal microscopy. **a-c**, Histograms of the colony height above the +1/2 defects (**a**, sample size $N = 437$), above the -1/2 defects (**b**, sample size $N = 384$), and from regions separated more than 9 μm from defects (**c**, sample size $N = 1000$). **d**, Illustrations of the polar tilt angle θ_p and the polar director $\mathbf{n}_p = \mathbf{n}\theta_p/|\theta_p|$ (top and middle panels), and that of the radial component of the polarity-induced force, $f_{p,r}$ (bottom panel). Since $\mathbf{f}_p^\pm \propto \theta_p^\pm \mathbf{n}$ with $\mathbf{n} = (\cos \psi, \sin \psi)$, we have $f_p^r \propto \theta_p |\cos(\phi - \psi)|$. **e,f**, Spatial profiles of the nematic tilt angle $\theta_n^\pm(\mathbf{r})$ for the +1/2 defects (**e**) and the -1/2 defects (**f**). The white rods represent the nematic director field $\mathbf{n}(\mathbf{r})$. **g,h**, $\theta_n^\pm |\cos(\phi - \psi)|$, which is proportional to the radial component of the polarity-induced force, $f_{p,r}$, around the +1/2 defect (**g**) and the -1/2 defect (**h**). The negative radial component indicates that the polarity-induced force is directed toward the defect. The black rods represent the nematic director field $\mathbf{n}(\mathbf{r})$. These are identical to Fig. 4e,f but reprinted here for comparison.



V. SUPPLEMENTARY MOVIE DESCRIPTIONS

Supplementary Movie 1:

A two-dimensional movie of a circular colony formed from a few cells (*E. coli*, MG1655) between a coverslip and an LB agar pad. The movie is played 600 times faster than the real speed.

Supplementary Movie 2:

A two-dimensional movie of a uniform colony formed from numerous cells (*E. coli*, MG1655) between a coverslip and an LB agar pad. Topological defects are also shown. The movie is played 600 times faster than the real speed.

Supplementary Movie 3:

A three-dimensional movie of a uniform colony formed from numerous cells (*E. coli*, MG1655-pZA3R-EYFP) between a coverslip and a TB+Cm agar pad. The movie is played at 8640 times faster than the real speed.

-
- [1] K. Kawaguchi, R. Kageyama, and M. Sano, *Nature* **545**, 327 (2017).
 - [2] K. Copenhagen, R. Alert, N. S. Wingreen, and J. W. Shaevitz, *Nat. Phys.* **17**, 211 (2021).
 - [3] L. M. Pismen, *Patterns and interfaces in dissipative dynamics* (Springer, 2006).
 - [4] L. M. Pismen, *Vortices in Nonlinear Fields. From Liquid Crystals to Superfluids. From Non-Equilibrium Patterns to Cosmic Strings* (Oxford University Press, 1999).
 - [5] Z. You, D. J. G. Pearce, A. Sengupta, and L. Giomi, *Phys. Rev. X* **8**, 031065 (2018).